Membrane curvature catalyzes lipid droplet assembly

Alexandre Santinho[1], Veijo T. Salo[2,3], Aymeric Chorlay[1], Shiqian Li[2,3], Xin Zhou[2,3], Mohyeddine Omrane[1], Elina Ikonen[2,3], Abdou Rachid Thiam[1]

[1] Laboratoire de Physique de l'École Normale Supérieure, ENS, Université PSL, CNRS, Sorbonne Université, Université de Paris, F-75005 Paris, France

[2] Department of Anatomy and Stem Cells and Metabolism Research Program, Faculty of Medicine, University of Helsinki, Helsinki, Finland

[3] Minerva Foundation Institute for Medical Research, Helsinki, Finland

(correspondence to thiam@ens.fr)

Abstract

Lipid droplet (LD) biogenesis begins in the endoplasmic reticulum (ER) bilayer, but how the ER topology impacts this process is unclear. An early step in LD formation is nucleation, wherein free neutral lipids, mainly triacylglycerols (TGs) and sterol esters (SEs), condense into a nascent LD. Here, we found that LDs preferably assemble at ER tubules, with higher curvature than ER sheets. Indeed, the presence of free TGs in tubules is energetically unfavorable, leading to outflow of TGs to flat regions or condensation into LDs. SEs inhibit the curvature-induced nucleation of TG LDs. Moreover, seipin enriched at ER tubules controls this condensation process, preventing excessive tubule-induced nucleation. The absence of seipin provokes erratic nucleation events determined by the abundance of ER tubules. On flat membranes, despite higher TG concentration, seipin cannot facilitate LD assembly. Our data indicate that curvature catalyzes LD assembly.

Highlights

- The presence of free TG molecules is unfavorable in curved membranes
- Membrane curvature facilitates but SEs inhibit the assembly of TG LDs
- ER topology modulates the number of assembled LDs
- Seipin controls the condensation of TG molecules into LDs at ER tubules

Introduction

Lipid droplets (LDs) are organelles at the center of cellular energy metabolism (Olzmann and Carvalho 2018). LDs consist of a neutral lipid (NL) oil core, mainly composed of triacylglycerols (TG) and/or sterol esters (SE), covered by a phospholipid monolayer containing proteins.

The biogenesis of LDs is triggered under various physiological conditions and proceeds via successive biochemical and biophysical reactions taking place at the endoplasmic reticulum (ER) (Chapman et al., 2019; Gao et al., 2019; Jackson, 2019; Walther et al., 2017). During conditions favoring lipid storage, these biochemical reactions mediate NL synthesis. NL oil molecules are encapsulated between the ER bilayer leaflets due to their hydrophobicity, and diffuse within the ER. When a critical concentration of NLs is reached, the molecules phase separate from the phospholipid bilayer and assemble into stabilized structures (Choudhary et al., 2015). This condensation and phase separation process, predicted by molecular dynamic simulations (Ben M'barek et al., 2017; Khandelia et al., 2010), is termed nucleation (Thiam and Beller, 2017; Thiam and Forêt, 2016). The nucleated condensate grows to become a nascent LD that buds into the cytosol (Olzmann and Carvalho, 2018; Salo and Ikonen, 2019; Walther et al., 2017). The extraction of LDs from the ER bilayer is influenced by membrane biophysical chemistry properties such as phospholipid composition, tension and shape, as well as proteins bound to the surface of the forming LD (Ben M'barek et al., 2017; Chorlay and Thiam, 2018; Chorlay et al., 2019; Choudhary et al., 2018; Deslandes et al., 2017; Zanghellini et al., 2010). For example, large membrane surface tensions, altered by phospholipids or membrane shape, will impede LD assembly and promote large LDs (Ben M'barek et al., 2017); membrane curvature and the recruitment of proteins or positively curved phospholipids to the outer ER membrane leaflet, favor external LD emergence (Chorlay et al., 2019; Choudhary et al., 2018; Zanghellini et al., 2010). However, how these factors impact on LD nucleation, i.e. assembly initiation, remains poorly understood. This is because nucleation happens at nanometric scales, making it difficult to investigate.

NLs condensate in a bilayer when they reach a critical concentration (Ben M'barek et al., 2017; Khandelia et al., 2010). This concentration is coupled to an energy barrier that likely depends on factors such as protein-lipid and lipid-lipid interactions, and membrane topology such as curvature (Thiam and Forêt, 2016). Topologically, the ER bilayer is made of sheets and tubules, whose relative abundance is affected by the cell type and phase (Puhka et al., 2007). Interestingly, LDs made of different NLs may arise at precise ER subregions (Hariri et al., 2018; Henne et al., 2019; Hsieh et al., 2012; Meyers et al., 2016; Nettebrock and Bohnert, 2019). It is currently unknown whether the ER topology or NL composition affects LD nucleation.

While many proteins affect the size and number of LDs, no single protein appears indispensable for LD formation. This is likely because NLs may behave as confined fluids that can spontaneously condense into droplets (Thiam and Forêt, 2016). However, it is crucial for cells to control such a condensation process to regulate LD assembly. A key protein implicated in LD assembly is seipin (Fei et al. 2008; Fei, Du, and Yang 2011; Henne, Reese, and Goodman 2018; Szymanski et al. 2007). It is an oligomeric ER membrane protein (Binns et al., 2010; Sui et al., 2018; Yan et al., 2018) whose dysfunction is linked to severe forms of lipodystrophy (Cartwright and Goodman, 2012; Fei et al., 2011; Magré et al., 2001) and neurological diseases (Guillén-Navarro et al., 2013; Ito and Suzuki, 2007; Windpassinger et al., 2004). Seipin oligomers are motile in the ER and arrest at sites where LDs emerge (Salo et al. 2016; Wang et al. 2016). At these sites, seipin is able to promote the growth of the newborn LDs and prevent their shrinkage by Ostwald ripening (Salo et al., 2019; Thiam and Forêt, 2016). How seipin acts in this process is still unclear but it might transfer TGs into forming LDs (Salo et al., 2019; Sui et al., 2018) and/or modulate the local phospholipid milieu (Pagac et al., 2016; Yan et al., 2018). In the absence of seipin, a phenotype of few supersized and many tiny LDs appears (Cartwright et al., 2015; Fei et al., 2008a; Salo et al., 2016; Wang et al., 2016). This tiny LD population is reduced by the concomitant depletion of Rab18 (Salo et al., 2019), another organizer of LD assembly (Xu et al., 2018).

Here, we found that the ER membrane curvature catalyzes LD assembly and LDs form at ER tubules. However, free TGs do not favor highly curved bilayers per se. Rather, curvature increases the chemical potential of TGs and upon increasing TG concentration in tubules, phase separation into LDs is triggered. Seipin is enriched at tubules, controlling LD assembly and facilitating TG flux to LDs. By this mechanism, seipin keeps the free TG level in the ER below a critical nucleation concentration. Without seipin, erratic nucleation events occur, controlled by the abundance of ER tubules.

Results

ER tubules are the sites of LD assembly and enriched in seipin

We previously reported that upon exogenous oleic acid (OA) administration to human A431 cells, LDs start to develop at ER domains marked by seipin (Salo et al., 2019). Indeed, in these cells, nascent LDs, visualized by the LD targeted model peptide LiveDrop-mCherry, appear at sites marked by endogenously fluorescently tagged seipin (**Figure 1A)**. Several studies have suggested ER tubules as the birthplace for LDs (Joshi et al., 2018; Kassan et al., 2013) but this has not been systematically investigated and the underlying principles remain unknown.

To investigate the relationship between LD formation and ER morphology, we utilized the machine-learning based image analysis software ilastik (Berg et al., 2019) to discern ER sheets and tubules from Airyscan live cell images of the ER visualized by the fluorescent ER marker BFP-KDEL. Using this analysis, we found that the sites of LD formation marked by seipin were highly enriched at ER tubules (**Figure 1A-B**). Of note, our ER segmentation method recapitulated the previously documented enrichment of known ER subdomain marker proteins at sheets or tubules (**S1A-C**) (Shibata et al., 2010; Voeltz et al., 2006). As a further validation of the analysis tool, we analyzed the ER morphology in control and Rab18 knockout (KO) cells. Rab18 KO has been reported to expand ER sheets at the expense of tubules in Cos7 cells (Gerondopoulos et al., 2014) and a similar phenotype was found in A431 cells (**Figure 1C**). Since Rab18 KO strongly reversed the tubule-to-sheet ratio (**Figure 1C**), we examined the sites of LD formation under this condition as compared to WT. To this end, we stringently delipidated the cells and then induced LD biogenesis by addition of OA, imaging cells during the first 15 min of LD biogenesis. We analyzed the localization of LDs marked by the LD540 dye and LD-associated seipins. Nascent LDs were enriched at ER tubules in both WT and Rab18 KO cells, despite the higher fraction of sheets in Rab18 KO cells **(Figures 1D-E)**.

As seipin can determine the site of LD formation (Salo et al., 2019) and LDs appeared to preferentially assemble at ER tubules, we investigated the localization of seipin in the ER. In live cell video recordings, seipin foci were highly motile in the ER, as previously reported (Salo et al., 2016; Wang et al., 2016). Often, when travelling via a sheet-like region, seipin appeared to move along the edges of the sheet **(Figure 1F)**, barely scanning the planar surface. Image analysis revealed seipin to be enriched at ER tubules **(Figure 1G)**. This enrichment was also apparent in Rab18 KO cells **(Figure 1G)**, even though these cells harbored less ER tubules (**Figure 1C**)**.**

To further investigate the localization of seipin in relation to membrane curvature, we worked with Cos7 cells transfected with sec61ß-mCherry and mouse YFP-seipin, which colocalized **(Figures 1H)**. We then induced the formation of large intra-cellular ER-derived vesicles by adding a hypotonic culture medium to the cells **(Figure S1D-E)** (Jaiswal et al., 2019; King et al., 2019). We observed the formation of numerous ER-vesicles of heterogeneous sizes, decorated by sec61ß-mCherry **(Figure 1H-I, S1E)**. We also captured situations where ER-vesicles co-existed with tubular structures **(Figure S1F)**. In this system, we found that the YFP-seipin signal was more intense on smaller ER-vesicles **(Figures 1I, S1E)** and tubules **(Figure S1F)** than on large ER-vesicles. By comparing the ratio of seipin to sec61ß signal, we observed an enrichment of seipin in smaller ER-vesicles **(Figure 1J)**. Similar results were obtained in HeLa cells (**Figures S1G-H**). These data suggest that seipin prefers regions of the ER with a higher curvature, and may act as a curvature sensor or be associated with one.

Overall, these data show that LD assembly is initiated at ER tubules, even when the tubular fraction is markedly decreased by Rab18 KO. Seipin is enriched at curved regions and may function as a nucleator of LDs at ER tubules.

LDs also nucleate at tubules in the absence of seipin

If seipin nucleates LDs at tubules, its depletion might alter this tubule-dependent nucleation of LDs. We thus investigated the sites of LD biogenesis in the absence of seipin. We used seipin-degron cells where seipin can be inducibly and rapidly depleted by the administration of indole-acetic-acid (IAA) (Li et al., 2019; Salo et al., 2019). IAA pre-treated seipin degron cells display dramatically altered LD formation, with a high number of tiny LDs and some supersized LDs appearing upon OA treatment (Salo et al., 2019). Remarkably, even in the absence of seipin, nascent LDs were enriched at ER tubules **(Figure 2A-B).** In both the absence and presence of seipin, this enrichment at ER tubules was more evident for smaller, apparently younger LDs **(Figure S2A-B)**.

To further study the contribution of curvature and seipin in LD nucleation, we took advantage of the heterogeneity of curvature in the ER-derived vesicles and probed LD assembly sites in this system. We used Cos7 cells transfected with mouse YFP-seipin, which were able to make LDs (**Figure S2C**). We next induced the formation of ER-vesicles and added the neutral lipid dye LipidTox. We then fed the cells with OA and red Bodipy-C_{12} OA (Bpy-C_{12}) (1000/1), previously shown to be incorporated into NLs (Rambold et al., 2015; Salo et al., 2019, 2016). Accordingly, Bpy-C_{12} became incorporated into new LipidTox-positive LDs (**Figure 2C, S2D)**, indicating that the swollen cells were capable of *de novo* LD formation, albeit slightly less efficiently than normal cells (**Figure S2D**). Interestingly, almost all generated Bpy-C_{12}-positive

LDs appeared near submicrometric seipin-positive vesicles (**Figure 2C-D, S2E**). We next performed similar experiments, transfecting the cells with YFP-seipin and sec61ß-mCherry (to mark the ER), and fed the cells with OA, using LipidTox to label the formed LDs. Upon this treatment, the majority of forming LDs were also found on submicrometric ER-vesicles (**Figure 2E-G**) or in tubules co-existing with large ER-vesicles (**Figures S2G**). The density of formed LDs per seipin signal was about 4-5 times higher at smaller ER-vesicles than at larger ones (**Figure 2H**). Indeed, LDs rarely appeared at larger ER-vesicles (**Figures 2C-F, S2G**) even though they contained clear seipin signal (**Figures 1J, 2C, 2I and S2G**). Thus, curvature seems to be required to facilitate LD formation in both the absence and presence of seipin.

We previously reported that relocalization of seipin to the nuclear envelope (NE) was sufficient to relocate LD biogenesis to this site (Salo et al., 2019). As the NE is a relatively flat membrane, this seemed at odds with our above observations suggesting that membrane curvature facilitates LD assembly. However, the GFP-nanobody based confinement will trap seipin to both the NE as well as nearby ER tubules, and distinguishing between these two possibilities is not possible at the light microscopy resolution **(Figure S2H).** To investigate this further, we transfected cells with seipin trapped at the NE with the ER-LD marker peptide HPos and imaged LD formation in live cells. Interestingly, we found that also in this situation virtually all LDs formed in close proximity to nearby ER tubules **(Figure S2I-J)**. Thus, LDs forming in the seipin NE-trapped cells may initially form at ER tubules in close proximity to the NE.

In summary, LDs preferentially form at ER tubules independently of seipin or the abundance of sheets. Regardless of seipin, the ER tubular shape seems to be crucial to facilitate LD assembly. Therefore, we hypothesize that membrane curvature may be sufficient and mandatory to efficiently trigger LD assembly.

TGs are diffusive in ER membranes and their distribution and assembly in LDs is curvature-dependent

Since LDs were mainly appearing from submicrometric ER-vesicles, we thought that maybe larger vesicles were not capable of making NLs. To test for this, we generated large ER-vesicles in Cos7 cells and added LipidTox. We then fed the cells with OA to drive NL production. We found an increase in LipidTox signal in the large ER-vesicles (**Figures 3A-B**), suggesting accumulation of NLs in the membrane. In model membranes, increasing the concentration of free TG indeed increased LipidTox signal (**Figure S3A**). This data suggests that the large ER-vesicles are able to synthesize free NLs.

We next used Bpy-C_{12} to better monitor the distribution of the NLs in ER-vesicles. Similar to red Bpy-C_{12}, also green Bpy-C_{12} was incorporated into NLs upon OA administration, mainly newly formed LDs, in both WT and swollen cells (**Figure S3B,C**). In addition, a uniform Bpy-C_{12} signal was observed in ER-vesicles (**Figures 3C-D, S3D**). Similar to LipidTox, also the Bpy- C_{12} signal increased over time, likely due to ongoing lipogenesis. This uniform Bpy-C_{12} signal rapidly recovered following photobleaching of a fraction of the membrane (**Figure 3E**), suggesting that the generated fluorescent NLs was freely diffusive in the membrane of the vesicle. Whilst Bpy-C_{12} is also known to be incorporated into phospholipids (REF: e.g. Salo 2016 EMBO J), the majority of the Bpy-C_{12} signal at ER-vesicles under these OA-induced lipogenic conditions circumstances likely stems from NLs, as the fluorescence intensity of Bpy-C_{12} was much lower in the plasma membrane (a phospholipid bilayer likely lacking NLs) than the at ER (a phospholipid bilayer likely harboring NLs) (**Figures S3E-I**).

We next focused on the NL level relative to ER-vesicle size. The concentration of Bpy-C_{12} signal was much higher in larger ER-vesicles compared to smaller ones, as measured by comparing Bpy-C_{12} to sec61-mCherry signal (**Figures 3F-G**). Large vesicles were thus not defective in NL synthesis as compared to smaller ones and instead appeared to harbor more NLs. However, as found in Figure 2, we again observed that most LDs formed at smaller, submicrometric ER-vesicles with lower Bpy-C_{12} membrane signal, rather than at the larger ER-vesicles with higher Bpy-C_{12} signal (**Figures 3H-I, S3J**). In line with this observation, HPos was also found on smaller vesicles (**Figure S3K**). These results suggest that despite a lower concentration of NL in the membrane, smaller ER-vesicles were more prone to support LD generation. This implies that the critical NL nucleation concentration may be lower on curved membranes compared to flat ones. This may also explain the inability of seipin to facilitate LD assembly at larger ER-vesicles (**Figure 2**).

In agreement with our above conclusion, the depletion of seipin and Pex30 in yeast leads to large onion ring-like ER membrane structures, low in curvature but full of free NLs (Wang et al., 2018). Analogously, our osmotic swelling treatment also lead to some cells with predominantly very similar appearing structures, rich in NLs but incapable of forming LDs (**Figure 3J**), despite the fact that all ER proteins are a priori present in the membranes. In comparison, in cells where submicrometric ER membranes were generated, LDs could be formed (**Figure 3K**).

Altogether, our data support the model that NLs synthesized in the ER membrane are initially freely diffusive. At a critical concentration, they condense into nascent LDs, phase separating from the bilayer. Our results suggest that flat membranes can accommodate a higher amount

of free NLs than curved membranes, implying that the critical concentration for nucleating LDs in flat areas is higher. This is possibly why seipin cannot decrease the energy barrier sufficiently to promote LD assembly at flat membranes. By sufficiently diminishing this critical NL concentration, membrane curvature may assist seipin to locally decrease the energy barrier and control LD nucleation.

The presence of TG but not SE is unfavorable in tubules

Our hypothesis required proof that membrane curvature modulates the distribution of TG molecules. We thus decided to study how NL distribution may be altered by membrane curvature in a protein-free system. We employed the droplet-embedded vesicle system (DEV), composed of an artificial LD (aLD) embedded in a giant unilamellar vesicle (GUV) (Chorlay and Thiam, 2018; Chorlay et al., 2019). We made TG aLDs containing 0.5% of TG-NBD to report for TG localization. The GUVs were made of dioleoylphosphatidylcholine containing 0.5% Rhodamine-DOPE (Rh-PE) to mark membranes, and 0.5% of biotinylated phospholipids, enabling us to pull out tubules. When DEVs were made under these conditions, the aLD was in equilibrium with free TG molecules in the bilayer (**Figure 4A**), similarly as seen in the ER-vesicles in (**Figures 3F)**. By using beads grafted with streptavidin and thereby binding biotinylated phospholipids, we pulled out tubules from the DEV and varied their radius by modulating the bilayer surface tension (Hochmuth and Evans, 1982) (**Figure 4B**).

When the radius of the tube was decreased, we observed a clear reduction in the TG/phospholipid ratio (**Figure 4C**). In other words, TG was more avidly excluded from the tubule to the flat membrane in comparison to phospholipids as curvature was increased (**Figures 4D-E, S4A**). To rule out artifacts induced by TG-NBD, we performed analogous experiments without TG-NBD, using Bodipy dye to label membrane hydrophobicity. The signal evolution of Bodipy in regards to curvature was similar to that of TG-NBD (**Figures S4B-C**). These data indicate that it is unfavorable for highly curved membranes to bear free TG molecules. Here, because the tubule is in equilibrium with a flat region, the TG molecules simply escape from tubules to the flat region where they seem to be of lower chemical potential. These findings are consistent with the TG distribution we previously found in ER-vesicles (**Figure 3F-G, J**).

We next compared the behavior of TG vs. SE in this system. We used a TG solution containing ~ 29.5% SE, the maximum solubility of SE in TG that we could attain at room temperature, and 0.5% SE-NBD (**Figures 4F-G and S4D-E**). Surprisingly, upon reduction of the tube radius, we found that the SE molecules remained on tubules and were relatively more enriched than phospholipids (**Figure 4G**). This is opposite to the behavior of TG alone (**Figure 4E**). To

visualize TG localization in this TG-SE mixture, we performed similar experiments but switching SE-NBD to TG-NBD (**Figures 4F, 4H and S4F**). In this situation, we found that TG was still excluded from tubules (**Figures 4H and S4F**). These data revealed that membrane curvature demixed the TG-SE mixture: TG molecules were sorted out to flat regions while SE remained slightly enriched in tubules. Thus, TG and SE have different chemical potentials in tubules vs. sheets.

The difference between TG and SE behavior in regards to membrane curvature was unexpected. To further study whether their dynamics were also differently altered, we simultaneously bleached both NBD and Rhodamine signals, reporting for NLs and phospholipids, respectively. Photobleaching was performed at the flat apex region of the DEV (**Figures S5A-C**) and on tubules (**Figures 5A-C**). On flat regions, we found that both TG and SE signals recovered faster than the phospholipid signal, indicating that SE and TG were both more mobile than phospholipids (**Figures 5D and S5B-C**). In contrast, in tubules TG was slightly less mobile than phospholipids, whilst SE still remained faster (**Figures 5B-D**). Thus, relative to phospholipid motility, curvature slows down TG but not SE.

Altogether, our above data revealed that the presence of independent TG molecules is unfavorable in curved regions. Furthermore, TG and SE have intrinsic static and dynamic behaviors discriminated by membrane curvature. They have different chemical potentials at flat and curved membrane areas. Thus, LD assembly mechanism likely depends on the NL composition.

Membrane curvature nucleates *in vitro* TG LDs

The presence of free TG molecules was more unfavorable in curved than flat regions (**Figure 4E**). Therefore, it could have been favorable for TG molecules to condense into droplets in tubules. However, TGs simply escaped from the tubule to the flat region, as they were part of a continuous system (**Figures 4C**). Under these static experimental conditions, there was no means by which to increase the concentration of TGs in tubules relative to phospholipids. In cells, ongoing lipogenesis guarantees that the concentration of TG in the ER membrane increases.

We reasoned that if we rapidly decreased the tube radius, faster than the NL diffusion time, we should be able to increase the local concentration of NL per phospholipid in the tube. Starting from a tube diameter of around 200 nm, the radius was rapidly decreased by drastically increasing the DEV bilayer tension (**Figure 5E**). We observed nucleation events whereby TG molecules condensed in the tubule into lens-like or droplet shapes, as reported

by TG-NBD or Bodipy signals (**Figures 5E-G, S5D-H**). The TG signal in these droplets was greater than that observed in the flat or tubular bilayer regions prior to nucleation (**Figures 5F and S5E,F,I**), supporting the notion that the TG molecules in the tubules had condensed. The success rate of nucleation increased with the decrease of the radius of the tubule (**Figure 5H**), either because the local concentration increased more or the effect of curvature was more pronounced. The nucleation of these model LDs was most often observed when the tube diameter was decreased to around 35 nm (**Figure 5H**), in the range of ER tubules (West et al., 2011).

Finally, as we had observed differences between TG and SE behavior in regards to membrane curvature, we repeated the previous experiment with a TG/SE (70/30) mixture. The success rate of nucleation in the presence of SE was much lower than that for TG alone (**Figure 5I**). These results suggest that membrane curvature more efficiently promotes the nucleation and assembly of TG- rather than SE-containing LDs. This divergence very likely pertains to the difference in chemical potential and mobility between the molecules (**Figures 4G-H and 5D**). TG, which diffused more slowly and was unfavored at tubules, was more efficiently assembled into droplets as the curvature was increased.

These data suggest that membrane curvature can solely mediate nucleation, especially of TG droplets. This is due to the higher chemical potential of TG in tubular regions, which is annihilated by the spontaneous condensation of TG molecules into droplets.

Modulating ER sheet-to-tubule ratio alters LD nucleation frequency in seipin deficient cells

Two main conclusions can be derived from our *in vitro* approach (**Figures 5H-I**). First, curvature increases the chemical potential of TG and thereby catalyzes LD assembly. Second, the presence of SE has an inhibitory contribution on the curvature-induced LD assembly. If our model is correct, modulating ER tubule-to-sheet ratio could affect the number of assembled LDs during NL synthesis, and this could be altered by SE levels. Since seipin interferes with LD nucleation, its presence might mask the contribution of membrane curvature. We therefore decided to work on a reductionist cell system lacking seipin, wherein cells generate a large amount of tiny LDs that fail to grow (Salo et al., 2016; Wang et al., 2016).

We first investigated the effect of increasing the amount of ER tubules. To this end, we stably transfected seipin degron cells with select ER tubule generating proteins: Reticulon 4 (Voeltz et al., 2006), Atlastin 1 (Hu et al., 2009) or Rab10 (English and Voeltz, 2013). We then acutely removed seipin and induced LD generation by OA. Seipin removal led to the drastic increase

of the tiny nucleated LDs, which could be efficiently rescued by the concomitant overexpression of seipin (**Figures 6A-B**). Overexpression of the tubule generating proteins increased the number of LDs in this system (**Figures 6A-B)**, suggesting that increasing tubules may enable higher number of LDs to be assembled.

We next studied the effect of increasing sheets at the expense of tubules. We previously observed that the number of *de novo* assembled LDs in seipin depleted cells is markedly reduced by Rab18 KO (Salo et al., 2019), which increases ER sheets (**Figure 1C**). This observation supports the notion that increasing sheets at the expense of tubules decreases nucleation events. To further investigate this, we depleted Rab10 with siRNAs or treated the cells with the microtubule polymerizing drug nocodazole, both of which induce ER sheet expansion (English and Voeltz, 2013; Joensuu et al., 2014). These manipulations efficiently reduced the number of tiny nucleated LDs in seipin depleted cells (**Figure 6C-D, S6A-B**). In the presence of seipin, increasing ER sheets only mildly reduced the number of assembled LDs (**Figure S6C-D**).

To investigate this phenomenon in more detail, we modulated the ER tubule-to-sheet ratio in seipin deficient cells and imaged them live during 45-75 min after OA administration. We modulated the sheet-to-tubule ratios by transient overexpression of mCherry-tagged ER shaping proteins CLIMP-63 or REEP-5, or soluble mCherry as control. We imaged peripheral ER regions with varying ER morphologies and found that regions of cells with higher ratios of tubules versus sheets tended to have more LDs (**Figure 6E-F**). Overall, these data suggest that the number of LDs generated in seipin deficient cells is linked to the ER-sheet-to-tubule ratio, with an increase in sheets lowering the number of LDs.

Our *in vitro* data suggested that SE have an inhibitory contribution to tubule-induced LD nucleation (**Figure 5I**). To test this hypothesis, we treated stringently starved cells with either 200 µM OA in the presence of SOAT1 inhibitor, to induce TG-enriched LDs, or 200 µM cholesterol-cyclodextrin in the presence of DGAT1 and DGAT2 inhibitors, to induce SE-enriched LDs, and imaged live nascent LDs. Despite equimolar lipid loading, OA induced a much higher number of LDs compared to cholesterol (**Figure 6G, S6E**), which agrees with our prediction, although we cannot rule out differences in efficiencies of the enzymes involved. Nascent SE-LDs were also more prevalent at ER tubules than sheets, albeit with a slight preference for sheets in comparison with TG-LDs **(Figure 6H-I)**. Finally, the number of LD assembly events in seipin-depleted cells could be increased by a concomitant treatment of cells with OA and SOAT1 inhibitor, i.e. by increasing the TG/SE ratio **(Figure 6J)**. These

observations are well in line with our *in vitro* data that TG LDs are more efficiently assembled than SE LDs and that SE has an inhibitory effect on LD nucleation.

Altogether, these data suggest that the number of TG LD assembly events is determined by the abundance of ER tubules in the absence of seipin and that seipin controls the number of LD assembly sites.

Discussion

Here, we studied the initial step of LD assembly, nucleation, which is the condensation of freely diffusing NL molecules. This process occurs when an energy barrier is crossed (**Figure 7A**) and this barrier is associated with a critical concentration of NLs (Thiam and Forêt, 2016). Our findings suggest that membrane curvature decreases this energy barrier and the associated critical concentration (**Figure 7A**). This happens because of the higher chemical potential of a free TG molecule in curved membranes. In this thermodynamic scenario, the increase of this chemical potential reduces the energy gap to the nucleation barrier. By doing so, membrane curvature catalyzes LD nucleation at tubules (**Figure 7A**).

The molecular mechanism by which membrane curvature increases the chemical potential of free TGs is unknown. Nonetheless, one of the major effects of curvature on membranes is to space phospholipids and to expose their hydrophobic core to water (**Figure 7B**). Thus, TG molecules might be more exposed to water molecules in a bilayer with higher curvature, thereby increasing the chemical potential of TG molecules. Consequently, to minimize free energy, TGs can escape from highly curved regions by diffusing to less curved ones, or by clustering and condensing into droplets (**Figure 7B**). Indeed, the latter situation minimizes the total free energy, similarly as when oil droplets merge to minimize the total oil/water contact area.

The thermodynamic framework underlining phase separation is well documented (Barrat and Hansen, 2003; Chandler, 2005; Safran, 2018), and we have previously described it in the context of LD assembly (Thiam and Forêt, 2016). It predicts that before the critical concentration for nucleation is reached, TG clusters appear and resorb rapidly, at a frequency increasing with the concentration of free TG (**Figure 7A**). The formation of such clusters would slow down TG diffusion, in line with our results indicating that membrane curvature reduces TG diffusion (**Figure 5B, 5D**). When the TG concentration reaches a critical nucleation concentration, larger clusters will transit into nascent LDs (**Figure 7A**). On flat membranes, this critical concentration is about 3-5% of free TG to phospholipids (Ben M'barek et al., 2017; Hamilton et al., 1983; Khandelia et al., 2010). On curved membranes, this value is expected to be smaller (**Figure 7A**). Consequently, membrane curvature should increase the frequency of appearance of unstable TG clusters, and hence the likelihood that they transit into stable, nascent LDs (**Figure 7C**). Such spontaneous process would lead to uncontrolled LD assembly, sporadically triggered at and by tubules.

Because seipin can dictate where LDs form (Salo et al., 2019) and control the number of LD assembly events on tubules (this study), seipin has to act very early to aid some clusters to jump the energy hill and transit into nascent LDs (**Figure 7A,C**). This is probably done in collaboration with its partners such as promethin in mammals, Ldo16/45 in yeast, or LDIP in plant *Arabidopsis* (Castro et al., 2019; Chung et al., 2019; Eisenberg-Bord et al., 2018; Pyc et al., 2017; Teixeira et al., 2018). Indeed, it has been recently shown that the seipin/promethin complex copurify with TG molecules (Chung et al., 2019), which could arise from TG clusters spontaneously formed at tubules. In the absence of seipin, and possibly of its partners, LD assembly would be controlled by curvature alone and the number of assembly event would be much larger (**Figure 6A, 7C**). Instead, seipin fosters some clusters and controls their transition into stable, nascent LDs (**Figure 7C**). Concretely, seipin may diffuse and detect some of the TG clusters in tubules and/or clusters might directly appear at seipin oligomers, since favorable protein-lipid interactions can trigger phase separation (Sens and Safran, 2000; Thiam and Forêt, 2016). In any case, by controlling the transition of few TG clusters into nascent LDs, seipin guarantees that only seipin-positive TG clusters get stabilized and grow. As these nascent LDs grow, the local concentration of free TG in the tubule decreases, inhibiting LD assembly close by (Salo et al., 2019). In the absence of seipin, much more TG clusters will transit into nascent LDs, controlled by the abundance of ER tubules (**Figure 6, 7C**).

Because the seipin can dictate where LDs form (Salo et al., 2019) and seipin controls the number of LD assembly events on tubules (this study), it has to act very early to aid some clusters to jump the energy hill and transit into nascent LDs (**Figure 7A,C**). Indeed, it has been recently shown that the seipin/promethin complex copurify with TG molecules (Chung et al., 2019), which could arise from TG clusters spontaneously formed at tubules. In the absence of seipin, LD assembly would be controlled by curvature alone and the number of assembly event would be much larger (**Figure 6A, 7C**). Instead, seipin fosters some clusters and controls their transition into stable, nascent LDs (**Figure 7C**). Concretely, seipin may diffuse and detect some of the TG clusters in tubules and/or clusters might directly appear at seipin oligomers, since favorable protein-lipid interactions can trigger phase separation (Sens and Safran, 2000; Thiam and Forêt, 2016). In any case, by controlling the transition of few TG clusters into nascent LDs, seipin guarantees that only seipin-positive TG clusters get stabilized and grow. As these nascent LDs grow, the local concentration of free TG in the tubule decreases, inhibiting LD assembly close by (Salo et al., 2019). In the absence of seipin, much more TG clusters will transit into nascent LDs, controlled by the abundance of ER tubules (**Figure 6, 7C**).

Interestingly, seipin collaborating proteins, from plant to human cells, seem to be membrane curvature sensors or inducers. These include the membrane shaping protein PEX30/MCTP2 (Joshi et al., 2018; Wang et al., 2018), promethin, Ldo16/45 (Eisenberg-Bord et al., 2018; Teixeira et al., 2018) and LDIP (Pyc et al., 2017). The induction of local curvature by these proteins could facilitate nucleation and trigger LD assembly at specific sites determined by seipin. Indeed, the concomitant depletion of Pex30 and seipin did not alter TG synthesis but rather their packaging into LDs, with TG molecules remaining in large onion-like multilamellar ER vesicles (Wang et al., 2018), similar as observed in **Figure 3J**. These structures are of almost zero curvature and are unable to make LDs. LDs did not efficiently form on large ER-vesicles (**Figure 2 and 3**) that contained abundant levels of seipin, suggesting that seipin activity in LD assembly relies on membrane curvature (**Figure 7C**).

In conclusion, we unveiled how NLs are distributed in membranes and found that membrane curvature catalyzes their assembly into LDs, in cooperation with seipin. Our results shed light on the role of ER topology on LD biogenesis and pave the way for further studies addressing how curvature is coupled to the function of seipin and other proteins regulating LD biogenesis.

Acknowledgements

We thank Anna Uro and Katharina Ven for excellent technical assistance, the Thiam team members and Dr. Lionel Fôret for their critical discussions and advice. This study was supported by the Academy of Finland (grants 282192, 312491, 307415 to E.I.), Sigrid Juselius Foundation (E.I.), and ANR-17-CE11-0003-NANODROP and ANR-18-CE11-0012-01-MOBIL to A.R.T. We thank Biocenter Finland and HiLIFE Light microscopy and Flow cytometry units. V.T.S. acknowledges support from the Finnish Medical, Paulo, Alfred Kordelin, Maud Kuistila, Biomedicum Helsinki, and Emil Aaltonen Foundation. A.S. is supported by Q-life program.

Author contribution

A.R.T., E.I., V.S. and A.S. designed experiments; A.S. performed *in vitro* and intra-cellular vesicle experiments, with the help of M.O. and A.C.; V.T.S. performed experiments in A431 cells with the help of S.L. and X.Z; A.R.T., E.I., V.S. and A.S. analyzed data and wrote the manuscript.

References

Barrat, J.-L., and Hansen, J.-P. (2003). Basic concepts for simple and complex liquids (Cambridge University Press).

Ben M'barek, K., Ajjaji, D., Chorlay, A., Vanni, S., Forêt, L., and Thiam, A.R. (2017). ER Membrane Phospholipids and Surface Tension Control Cellular Lipid Droplet Formation. Dev. Cell *41*, 591-604.e7.

Berg, S., Kutra, D., Kroeger, T., Straehle, C.N., Kausler, B.X., Haubold, C., Schiegg, M., Ales, J., Beier, T., and Rudy, M. (2019). ilastik: interactive machine learning for (bio) image analysis. Nat. Methods 1–7.

Binns, D., Lee, S., Hilton, C.L., Jiang, Q.-X., and Goodman, J.M. (2010). Seipin is a discrete homooligomer. Biochemistry *49*, 10747–10755.

Cartwright, B.R., and Goodman, J.M. (2012). Seipin: from human disease to molecular mechanism. J. Lipid Res. *53*, 1042–1055.

Cartwright, B.R., Binns, D.D., Hilton, C.L., Han, S., Gao, Q., and Goodman, J.M. (2015). Seipin performs dissectible functions in promoting lipid droplet biogenesis and regulating droplet morphology. Mol. Biol. Cell *26*, 726–739.

Castro, I.G., Eisenberg-Bord, M., Persiani, E., Rochford, J.J., Schuldiner, M., and Bohnert, M. (2019). Promethin Is a Conserved Seipin Partner Protein. Cells *8*, 268.

Chandler, D. (2005). Interfaces and the driving force of hydrophobic assembly. Nature *437*, 640.

Chapman, K.D., Aziz, M., Dyer, J.M., and Mullen, R.T. (2019). Mechanisms of lipid droplet biogenesis. Biochem. J. *476*, 1929–1942.

Chorlay, A., and Thiam, A.R. (2018). An asymmetry in monolayer tension regulates lipid droplet budding direction. Biophys. J. *114*, 631–640.

Chorlay, A., Monticelli, L., Ferreira, J.V., M'barek, K.B., Ajjaji, D., Wang, S., Johnson, E., Beck, R., Omrane, M., Beller, M., et al. (2019). Membrane Asymmetry Imposes Directionality on Lipid Droplet Emergence from the ER. Dev. Cell *0*.

Choudhary, V., Ojha, N., Golden, A., and Prinz, W.A. (2015). A conserved family of proteins facilitates nascent lipid droplet budding from the ER. J Cell Biol *211*, 261–271.

Choudhary, V., Golani, G., Joshi, A.S., Cottier, S., Schneiter, R., Prinz, W.A., and Kozlov, M.M. (2018). Architecture of lipid droplets in endoplasmic reticulum is determined by phospholipid intrinsic curvature. Curr. Biol. *28*, 915–926.

Chung, J., Wu, X., Lambert, T.J., Lai, Z.W., Walther, T.C., and Farese Jr, R.V. (2019). LDAF1 and Seipin Form a Lipid Droplet Assembly Complex. Dev. Cell.

Deslandes, F., Thiam, A.R., and Forêt, L. (2017). Lipid Droplets Can Spontaneously Bud Off from a Symmetric Bilayer. Biophys. J. *113*, 15–18.

Eisenberg-Bord, M., Mari, M., Weill, U., Rosenfeld-Gur, E., Moldavski, O., Castro, I.G., Soni, K.G., Harpaz, N., Levine, T.P., and Futerman, A.H. (2018). Identification of seipin-linked factors that act as determinants of a lipid droplet subpopulation. J Cell Biol *217*, 269–282.

English, A.R., and Voeltz, G.K. (2013). Rab10 GTPase regulates ER dynamics and morphology. Nat. Cell Biol. *15*, 169.

Fei, W., Shui, G., Gaeta, B., Du, X., Kuerschner, L., Li, P., Brown, A.J., Wenk, M.R., Parton, R.G., and Yang, H. (2008a). Fld1p, a functional homologue of human seipin, regulates the size of lipid droplets in yeast. J Cell Biol *180*, 473–482.

Fei, W., Shui, G., Gaeta, B., Du, X., Kuerschner, L., Li, P., Brown, a. J., Wenk, M.R., Parton, R.G., and Yang, H. (2008b). Fld1p, a functional homologue of human seipin, regulates the size of lipid droplets in yeast. J. Cell Biol. *180*, 473–482.

Fei, W., Du, X., and Yang, H. (2011). Seipin, adipogenesis and lipid droplets. Trends Endocrinol. Metab. *22*, 204–210.

Friedman, J.R., Lackner, L.L., West, M., DiBenedetto, J.R., Nunnari, J., and Voeltz, G.K. (2011). ER tubules mark sites of mitochondrial division. Science *334*, 358–362.

Gao, M., Huang, X., Song, B.-L., and Yang, H. (2019). The biogenesis of lipid droplets: Lipids take center stage. Prog. Lipid Res. 100989.

Gerondopoulos, A., Bastos, R.N., Yoshimura, S., Anderson, R., Carpanini, S., Aligianis, I., Handley, M.T., and Barr, F.A. (2014). Rab18 and a Rab18 GEF complex are required for normal ER structure. J Cell Biol *205*, 707–720.

Goldstein, J.L., Basu, S.K., and Brown, M.S. (1983). Receptor-mediated endocytosis of low-density lipoprotein in cultured cells. Methods Enzymol. *VOL. 98*, 241–260.

Guillén-Navarro, E., Sánchez-Iglesias, S., Domingo-Jiménez, R., Victoria, B., Ruiz-Riquelme, A., Rábano, A., Loidi, L., Beiras, A., González-Méndez, B., and Ramos, A. (2013). A new seipin-associated neurodegenerative syndrome. J. Med. Genet. *50*, 401–409.

Hamilton, J.A., Miller, K.W., and Small, D.M. (1983). Solubilization of triolein and cholesteryl oleate in egg phosphatidylcholine vesicles. J. Biol. Chem. *258*, 12821–12826.

Hariri, H., Rogers, S., Ugrankar, R., Liu, Y.L., Feathers, J.R., and Henne, W.M. (2018). Lipid droplet biogenesis is spatially coordinated at ER–vacuole contacts under nutritional stress. EMBO Rep. *19*, 57–72.

Henne, M., Goodman, J.M., and Hariri, H. (2019). Spatial compartmentalization of lipid droplet biogenesis. Biochim. Biophys. Acta BBA-Mol. Cell Biol. Lipids.

Henne, W.M., Reese, M.L., and Goodman, J.M. (2018). The assembly of lipid droplets and their roles in challenged cells. EMBO J. *37*, e98947.

Hochmuth, R.M., and Evans, E.A. (1982). Extensional flow of erythrocyte membrane from cell body to elastic tether. I. Analysis. Biophys. J. *39*, 71–81.

Hölttä-Vuori, M., Salo, V.T., Ohsaki, Y., Suster, M.L., and Ikonen, E. (2013). Alleviation of seipinopathy-related ER stress by triglyceride storage. Hum. Mol. Genet. *22*, 1157–1166.

Hsieh, K., Lee, Y.K., Londos, C., Raaka, B.M., Dalen, K.T., and Kimmel, A.R. (2012). Perilipin family members preferentially sequester to either triacylglycerol-specific or cholesteryl-ester-specific intracellular lipid storage droplets. J Cell Sci *125*, 4067–4076.

Hu, J., Shibata, Y., Zhu, P.-P., Voss, C., Rismanchi, N., Prinz, W.A., Rapoport, T.A., and Blackstone, C. (2009). A class of dynamin-like GTPases involved in the generation of the tubular ER network. Cell *138*, 549–561.

Ito, D., and Suzuki, N. (2007). Molecular pathogenesis of seipin/BSCL2-related motor neuron diseases. Ann. Neurol. Off. J. Am. Neurol. Assoc. Child Neurol. Soc. *61*, 237–250.

Jackson, C.L. (2019). Lipid droplet biogenesis. Curr. Opin. Cell Biol. *59*, 88–96.

Jaiswal, A., Hoerth, C.H., Pereira, A.M.Z., and Lorenz, H. (2019). Improved spatial resolution by induced live cell and organelle swelling in hypotonic solutions. Sci. Rep. *9*, 1–13.

Joensuu, M., Belevich, I., Rämö, O., Nevzorov, I., Vihinen, H., Puhka, M., Witkos, T.M., Lowe, M., Vartiainen, M.K., and Jokitalo, E. (2014). ER sheet persistence is coupled to myosin 1c–regulated dynamic actin filament arrays. Mol. Biol. Cell *25*, 1111–1126.

Joshi, A.S., Nebenfuehr, B., Choudhary, V., Satpute-Krishnan, P., Levine, T.P., Golden, A., and Prinz, W.A. (2018). Lipid droplet and peroxisome biogenesis occur at the same ER subdomains. Nat. Commun. *9*, 2940.

Kassan, A., Herms, A., Fernández-Vidal, A., Bosch, M., Schieber, N.L., Reddy, B.J., Fajardo, A., Gelabert-Baldrich, M., Tebar, F., and Enrich, C. (2013). Acyl-CoA synthetase 3 promotes lipid droplet biogenesis in ER microdomains. J Cell Biol *203*, 985–1001.

Khandelia, H., Duelund, L., Pakkanen, K.I., and Ipsen, J.H. (2010). Triglyceride blisters in lipid bilayers: implications for lipid droplet biogenesis and the mobile lipid signal in cancer cell membranes. PloS One *5*, e12811.

King, C., Sengupta, P., Seo, A., and Lippincott-Schwartz, J. (2019). ER membranes exhibit phase behavior at sites of organelle contact. BioRxiv 707505.

Li, S., Prasanna, X., Salo, V.T., Vattulainen, I., and Ikonen, E. (2019). An efficient auxin-inducible degron system with low basal degradation in human cells. Nat. Methods *16*, 866–869.

Magré, J., Delépine, M., Khallouf, E., Gedde-Dahl Jr, T., Van Maldergem, L., Sobel, E., Papp, J., Meier, M., Mégarbané, A., and Lathrop, M. (2001). Identification of the gene altered in Berardinelli–Seip congenital lipodystrophy on chromosome 11q13. Nat. Genet. *28*, 365.

Meyers, A., del Rio, Z.P., Beaver, R.A., Morris, R.M., Weiskittel, T.M., Alshibli, A.K., Mannik, J., Morrell-Falvey, J., and Dalhaimer, P. (2016). Lipid droplets form from distinct regions of the cell in the fission yeast Schizosaccharomyces pombe. Traffic *17*, 657–669.

Nettebrock, N.T., and Bohnert, M. (2019). Born this way–Biogenesis of lipid droplets from specialized ER subdomains. Biochim. Biophys. Acta BBA-Mol. Cell Biol. Lipids.

Olzmann, J.A., and Carvalho, P. (2018). Dynamics and functions of lipid droplets. Nat. Rev. Mol. Cell Biol. 1.

Pagac, M., Cooper, D.E., Qi, Y., Lukmantara, I.E., Mak, H.Y., Wu, Z., Tian, Y., Liu, Z., Lei, M., and Du, X. (2016). SEIPIN regulates lipid droplet expansion and adipocyte development by modulating the activity of glycerol-3-phosphate acyltransferase. Cell Rep. *17*, 1546–1559.

Puhka, M., Vihinen, H., Joensuu, M., and Jokitalo, E. (2007). Endoplasmic reticulum remains continuous and undergoes sheet-to-tubule transformation during cell division in mammalian cells. J. Cell Biol. *179*, 895–909.

Pyc, M., Cai, Y., Gidda, S.K., Yurchenko, O., Park, S., Kretzschmar, F.K., Ischebeck, T., Valerius, O., Braus, G.H., and Chapman, K.D. (2017). Arabidopsis lipid droplet-associated protein (LDAP)–interacting protein (LDIP) influences lipid droplet size and neutral lipid homeostasis in both leaves and seeds. Plant J. *92*, 1182–1201.

Rambold, A.S., Cohen, S., and Lippincott-Schwartz, J. (2015). Fatty acid trafficking in starved cells: regulation by lipid droplet lipolysis, autophagy, and mitochondrial fusion dynamics. Dev. Cell *32*, 678–692.

Safran, S. (2018). Statistical thermodynamics of surfaces, interfaces, and membranes (CRC Press).

Salo, V.T., and Ikonen, E. (2019). Moving out but keeping in touch: contacts between endoplasmic reticulum and lipid droplets. Curr. Opin. Cell Biol. *57*, 64–70.

Salo, V., Li, S., Vihinen, H., Hölttä-Vuori, M., Szkalisity, A., Horvath, P., Belevich, I., Peränen, J., Thiele, C., Somerharju, P., et al. (2019). Seipin facilitates triglyceride flow to lipid droplet and counteracts droplet ripening via ER contact. Dev. Cell *50*, 1–16.

Salo, V.T., Belevich, I., Li, S., Karhinen, L., Vihinen, H., Vigouroux, C., Magré, J., Thiele, C., Hölttä-Vuori, M., and Jokitalo, E. (2016). Seipin regulates ER–lipid droplet contacts and cargo delivery. EMBO J. *35*, 2699–2716.

Sens, P., and Safran, S.A. (2000). Inclusions induced phase separation in mixed lipid film. Eur. Phys. J. E *1*, 237–248.

Shibata, Y., Shemesh, T., Prinz, W.A., Palazzo, A.F., Kozlov, M.M., and Rapoport, T.A. (2010). Mechanisms determining the morphology of the peripheral ER. Cell *143*, 774–788.

Spandl, J., White, D.J., Peychl, J., and Thiele, C. (2009). Live cell multicolor imaging of lipid droplets with a new dye, LD540. Traffic Cph. Den. *10*, 1579–1584.

Sui, X., Arlt, H., Brock, K.P., Lai, Z.W., DiMaio, F., Marks, D.S., Liao, M., Farese, R.V., and Walther, T.C. (2018). Cryo–electron microscopy structure of the lipid droplet–formation protein seipin. J Cell Biol *217*, 4080–4091.

Szymanski, K.M., Binns, D., Bartz, R., Grishin, N.V., Li, W.-P., Agarwal, A.K., Garg, A., Anderson, R.G., and Goodman, J.M. (2007). The lipodystrophy protein seipin is found at

endoplasmic reticulum lipid droplet junctions and is important for droplet morphology. Proc. Natl. Acad. Sci. *104*, 20890–20895.

Teixeira, V., Johnsen, L., Martínez-Montañés, F., Grippa, A., Buxó, L., Idrissi, F.-Z., Ejsing, C.S., and Carvalho, P. (2018). Regulation of lipid droplets by metabolically controlled Ldo isoforms. J Cell Biol *217*, 127–138.

Thiam, A.R., and Beller, M. (2017). The why, when and how of lipid droplet diversity. J Cell Sci *130*, 315–324.

Thiam, A.R., and Dugail, I. (2019). Lipid droplet–membrane contact sites–from protein binding to function. J. Cell Sci. *132*, jcs230169.

Thiam, A.R., and Forêt, L. (2016). The physics of lipid droplet nucleation, growth and budding. Biochim. Biophys. Acta *1861*, 715–722.

Thiam, A.R., Antonny, B., Wang, J., Delacotte, J., Wilfling, F., Walther, T.C., Beck, R., Rothman, J.E., and Pincet, F. (2013). COPI buds 60-nm lipid droplets from reconstituted water–phospholipid–triacylglyceride interfaces, suggesting a tension clamp function. Proc. Natl. Acad. Sci. *110*, 13244–13249.

Voeltz, G.K., Prinz, W.A., Shibata, Y., Rist, J.M., and Rapoport, T.A. (2006). A class of membrane proteins shaping the tubular endoplasmic reticulum. Cell *124*, 573–586.

Walther, T.C., Chung, J., and Farese Jr, R.V. (2017). Lipid droplet biogenesis. Annu. Rev. Cell Dev. Biol. *33*, 491–510.

Wang, H., Becuwe, M., Housden, B.E., Chitraju, C., Porras, A.J., Graham, M.M., Liu, X.N., Thiam, A.R., Savage, D.B., and Agarwal, A.K. (2016). Seipin is required for converting nascent to mature lipid droplets. Elife *5*, e16582.

Wang, S., Idrissi, F.-Z., Hermansson, M., Grippa, A., Ejsing, C.S., and Carvalho, P. (2018). Seipin and the membrane-shaping protein Pex30 cooperate in organelle budding from the endoplasmic reticulum. Nat. Commun. *9*, 2939.

Welte, M.A., and Gould, A.P. (2017). Lipid droplet functions beyond energy storage. Biochim. Biophys. Acta Mol. Cell Biol. Lipids *1862*, 1260–1272.

West, M., Zurek, N., Hoenger, A., and Voeltz, G.K. (2011). A 3D analysis of yeast ER structure reveals how ER domains are organized by membrane curvature. J. Cell Biol. *193*, 333–346.

Windpassinger, C., Auer-Grumbach, M., Irobi, J., Patel, H., Petek, E., Hörl, G., Malli, R., Reed, J.A., Dierick, I., and Verpoorten, N. (2004). Heterozygous missense mutations in BSCL2 are associated with distal hereditary motor neuropathy and Silver syndrome. Nat. Genet. *36*, 271.

Xu, D., Li, Y., Wu, L., Li, Y., Zhao, D., Yu, J., Huang, T., Ferguson, C., Parton, R.G., and Yang, H. (2018). Rab18 promotes lipid droplet (LD) growth by tethering the ER to LDs through SNARE and NRZ interactions. J Cell Biol *217*, 975–995.

Yan, R., Qian, H., Lukmantara, I., Gao, M., Du, X., Yan, N., and Yang, H. (2018). Human SEIPIN binds anionic phospholipids. Dev. Cell *47*, 248–256.

Zanghellini, J., Wodlei, F., and Von Grünberg, H.H. (2010). Phospholipid demixing and the birth of a lipid droplet. J. Theor. Biol. *264*, 952–961.

Zurek, N., Sparks, L., and Voeltz, G. (2011). Reticulon short hairpin transmembrane domains are used to shape ER tubules. Traffic *12*, 28–41.

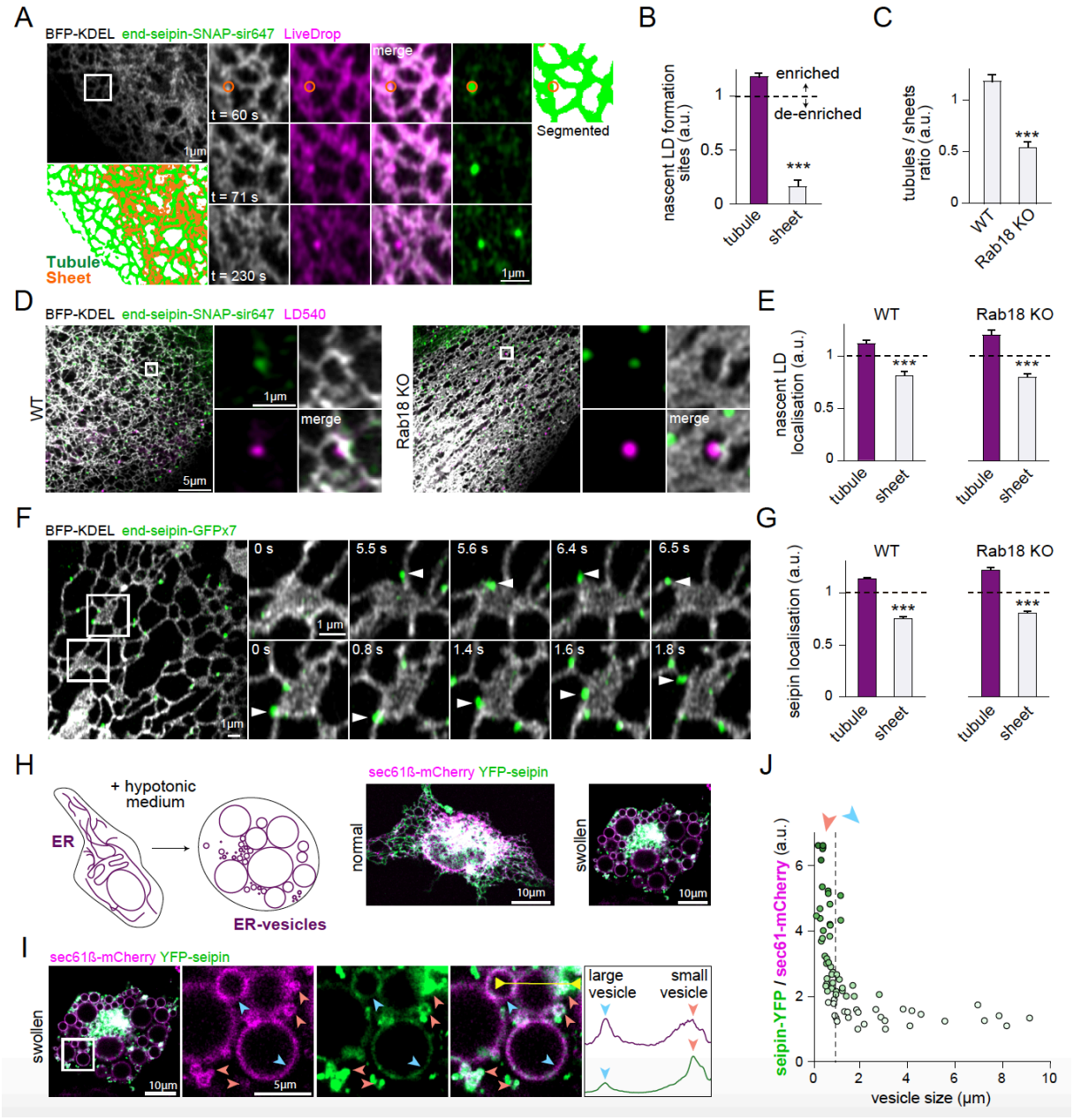

Figure 1. LDs are generated at ER tubules where seipin is enriched

A) A431 cells with seipin tagged endogenously with GFPx7 (end-seipin-GFPx7) and stably expressing BFP-KDEL and LiveDrop-mCherry were delipidated (1 d LPDS) and imaged live with Airyscan microscopy, starting 50 s after OA loading. ER tubules and sheets were segmented as described in Materials and methods. Insets show an example of an emerging LD, circle denotes ROI marked by seipin, used for analysis in B.

B) Analysis of nascent LD formation sites from A, the distribution of segmented ER pixels at LD-associated seipin foci prior to LiveDrop accumulation was analyzed and compared to overall pixel distribution of sheets/tubules in the same cells. Bars: mean +/- SEM, n= 24 LDs, 6 cells, 2 experiments.

C) WT and Rab 18 KO cells stably expressing BFP-KDEL cells were imaged live, the ER was segmented and analyzed. Bars: mean +/- SEM, n= 61 ROIs from 61 cells/genotype, 3 experiments.

D) A431 WT and Rab18 KO cells with seipin tagged endogenously with SNAPf-tag and stably expressing BFP-KDEL were delipidated (3 d LPDS, 18 h DGATi) and seipin was stained with SIR647 4-6 h prior to imaging. After DGATi washout, OA, SOAT1 inhibitor and LD540 were added to the cells and they were imaged live 0-15 min after OA addition.

E) Analysis of D. The distribution of segmented ER pixels at LD-associated seipin foci was compared to overall pixel distribution of sheets/tubules in the same cells. Bars: mean +/- SEM, n= 25-38 ROIs from 25-38 cells, 2-3 experiments (>800 LD-associated seipins/genotype).

F) end-seipin-GFPx7 cells stably expressing BFP-KDEL were imaged live. Seipin is enriched at ER tubules and when moving through sheet regions (insets) prefers the edges of sheets.

G) end-seipin-GFPx7 cells stably expressing BFP-KDEL with or without Rab18 KO were imaged live by Airyscan microscopy and the distribution of segmented ER pixels at each seipin ROI was compared to overall pixel distribution of sheets/tubules in the same cells. Bars: mean +/- SEM, n= 25-38 ROIs from 25-38 cells, 2-3 experiments (> 9000 seipin foci/genotype).

H) Schematic representation of the ER-vesicles formation with swollen cells. Left: Cos7 cell expressing sec61ß-mCherry and YFP-seipin was imaged live by confocal microscopy**.** Right: a Cos7 cell expressing sec61ß-mCherry and YFP-seipin was imaged live 10 min after ER-vesicle formation.

I) Cos7 cell expressing sec61ß-mCherry and YFP-seipin were imaged live 10 min after ER-vesicle formation. Submicrometric ER-vesicles (red arrows) display brighter YFP-seipin signal than larger vesicles (blue arrows). Line scan over two ER-vesicles (yellow line) displays brighter signal for the small vesicle.

J) Analysis of I. The fluorescence intensity ratio of YFP-seipin and sec61ß-mCherry is plotted relative to vesicle size, indicating seipin is enriched on submicrometric vesicles, n= 69 vesicles, 3 experiments.

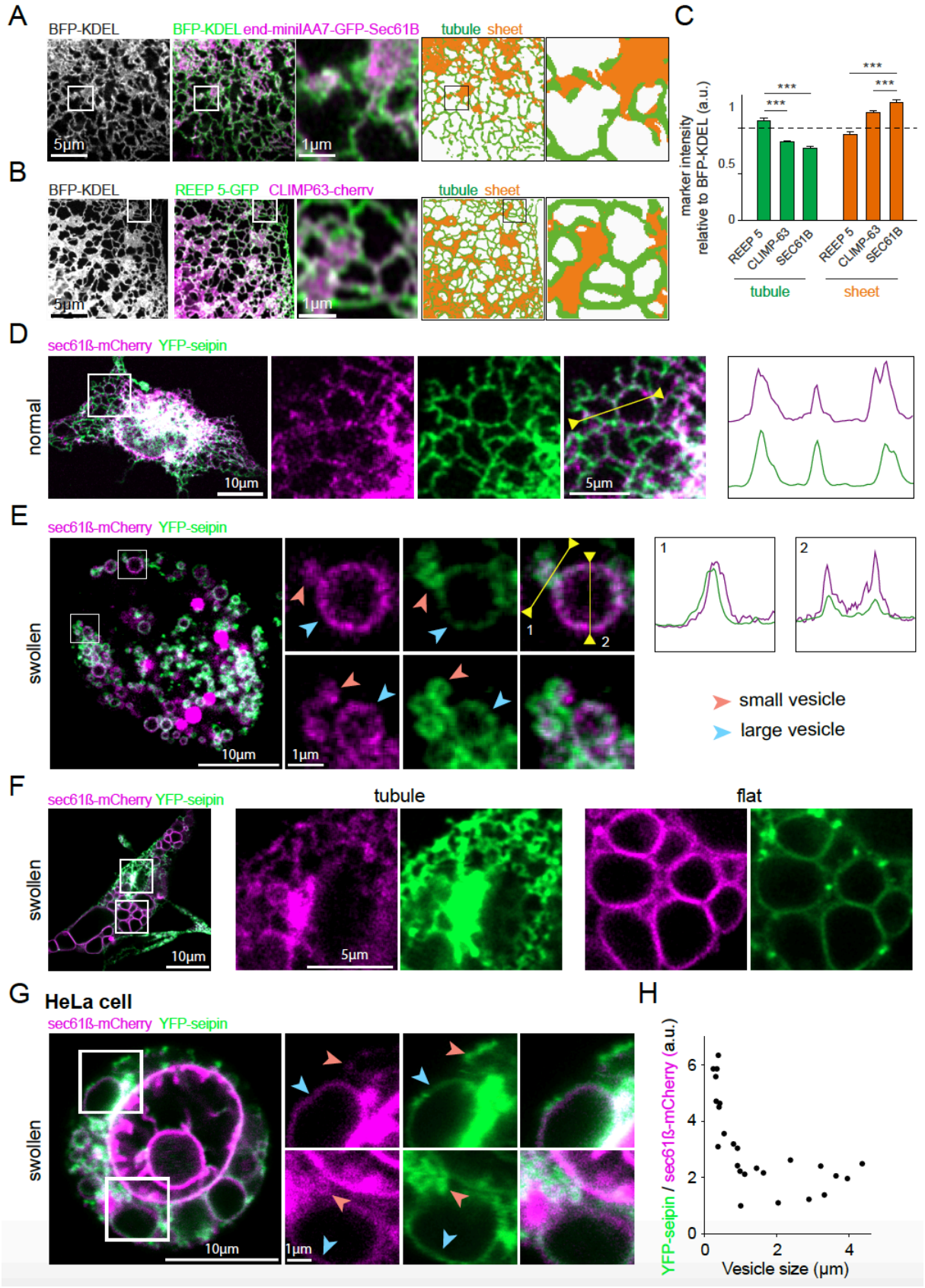

Figure S1: related to figure 1

A-C) Validation of the ER segmentation tool.

A) A431 cells with sec61ß tagged endogenously with miniIAA7-GFP and stably expressing BFP-KDEL were imaged live by Airyscan microscopy. The ER was segmented into sheets and tubules using the BFP-KDEL channel.

B) A431 cells stably expressing BFP-KDEL were transfected with REEP 5-GFP and CLIMP63-mCherry for 1 d and imaged live by Airyscan microscopy. The ER was segmented into sheets and tubules using the BFP-KDEL channel.

C) Analysis of A and B. For each cell, the fluorescence intensity ratio of BFP-KDEL at tubules and sheets was compared to the fluorescence intensity ratios of the various ER subdomain markers at tubules and sheets, bars: mean +/- SEM, n= 45-46 ROIs from 45-46 cells, 2 experiments.

D) Cos7 cells expressing sec61ß-mCherry and YFP-seipin were imaged live by confocal microscopy. A line scan (yellow line) of the fluorescence intensity profiles show same maxima localization.

E) Related to Figure 1I, additional examples of swollen Cos7 cells expressing sec61ß-mCherry and YFP-seipin, imaged 10 min after ER-vesicle formation. Submicrometric (red arrows) show brighter YFP-seipin signal than larger ER-vesicles (blue arrows). Line scans (yellow lines) on two ER-vesicles of different sizes.

F) Cos7 cells expressing sec61ß-mCherry and YFP-seipin were imaged 10 min after swelling. An exemplary snapshot is shown of a cell wherein ER tubules co-exist with large vesicular regions (“flat”).

G) Swollen HeLa cells expressing sec61ß-mCherry and YFP-seipin were imaged 10 min after ER-vesicle formation. Submicrometric (red arrows) show brighter YFP-seipin signal than larger ER-vesicles (blue arrows).

H) Analysis of G. The fluorescence intensity ratio of YFP-seipin and sec61ß-mCherry is plotted relative to vesicle size, indicating seipin is enriched on submicrometric vesicles, n= 2 cells, 2 experiments, 25 vesicles.

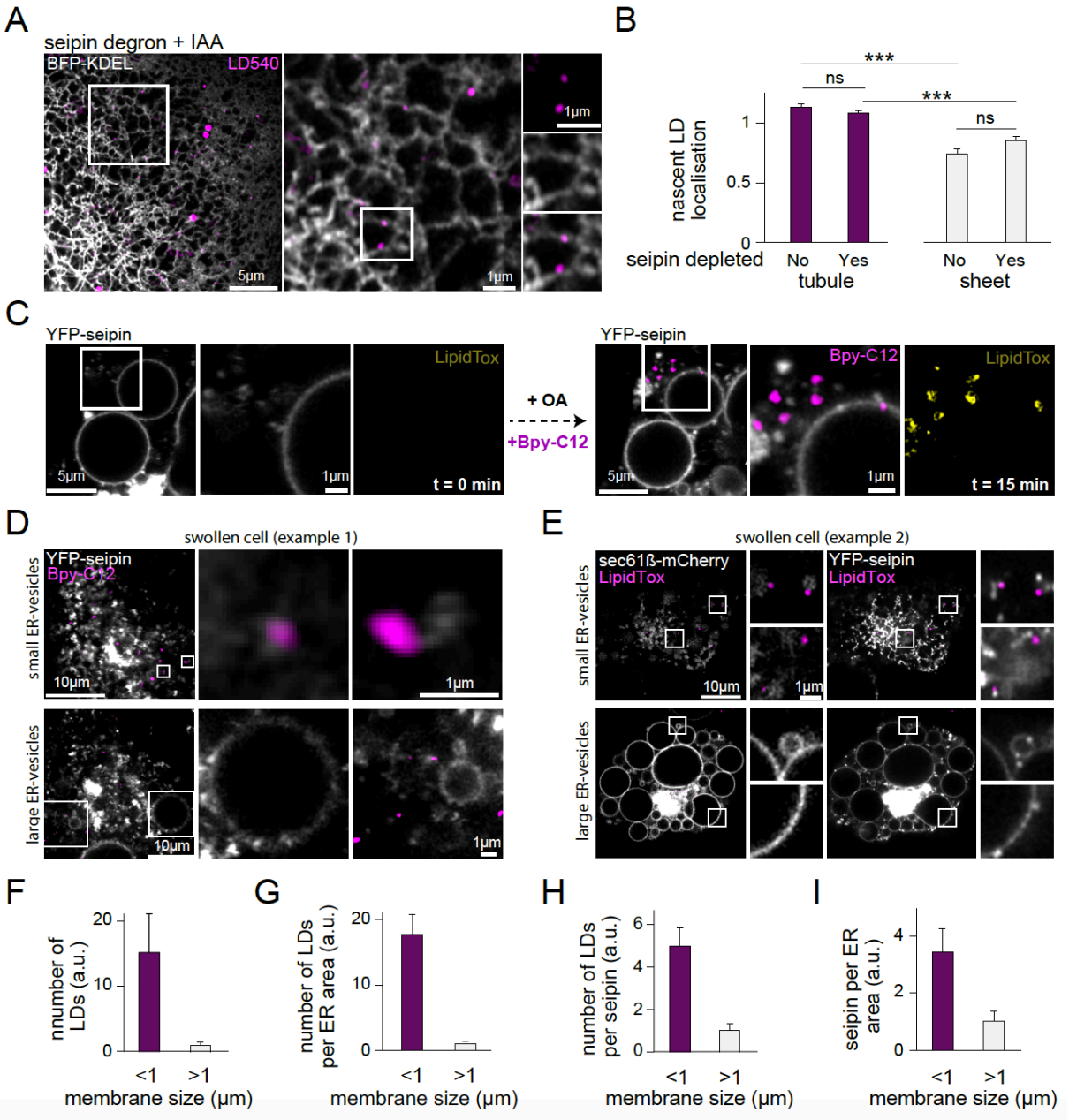

Figure 2. LDs nucleate at ER tubules in the absence of seipin and not at large vesicles in the presence of seipin

A) Seipin degron cells were treated and imaged as in Figure 1D. Seipin was depleted by adding IAA to the cells 18 h prior to imaging.

B) Analysis of A. The distribution of segmented ER pixels at nascent LDs was compared to overall pixel distribution of sheets/tubules in the same cells. Bars: mean +/- SEM, n= 44-47 ROIs from 44-47 cells, 2 experiments (> 1000 LDs/group).

C) Swollen Cos7 cells were imaged before and after OA and Bpy-C_{12} addition. Note Bpy-C_{12} and LipidTox colocalization in LDs.

D) ER-vesicles were induced in Cos7 cells expressing YFP-seipin and sec61ß-mCherry and imaged 15 min after OA addition. Note submicrometric ER-vesicles apposed to LDs.

E) ER-vesicles were induced in Cos7 cells expressing YFP-seipin and sec61ß-mCherry and imaged 15 min after OA addition.
F) Analysis of D and E. LD number per ER-vesicle size in swollen cells overexpressing seipin. Mean +/- SEM; n = 1230 LDs from 5 cells, 4 experiments.
G) Analysis of D and E. LD number per ER-vesicle size in F is normalized to sec61ß signal, defined as the number of LDs per ER surface area.
H) Analysis of D and E. Number of LDs normalized to seipin signal per ER-vesicle size, defined as the number of LDs per seipin signal.
I) Analysis of D and E. Seipin intensity per ER-vesicle, normalized to sec61ß signal, defined as seipin signal per ER surface area.

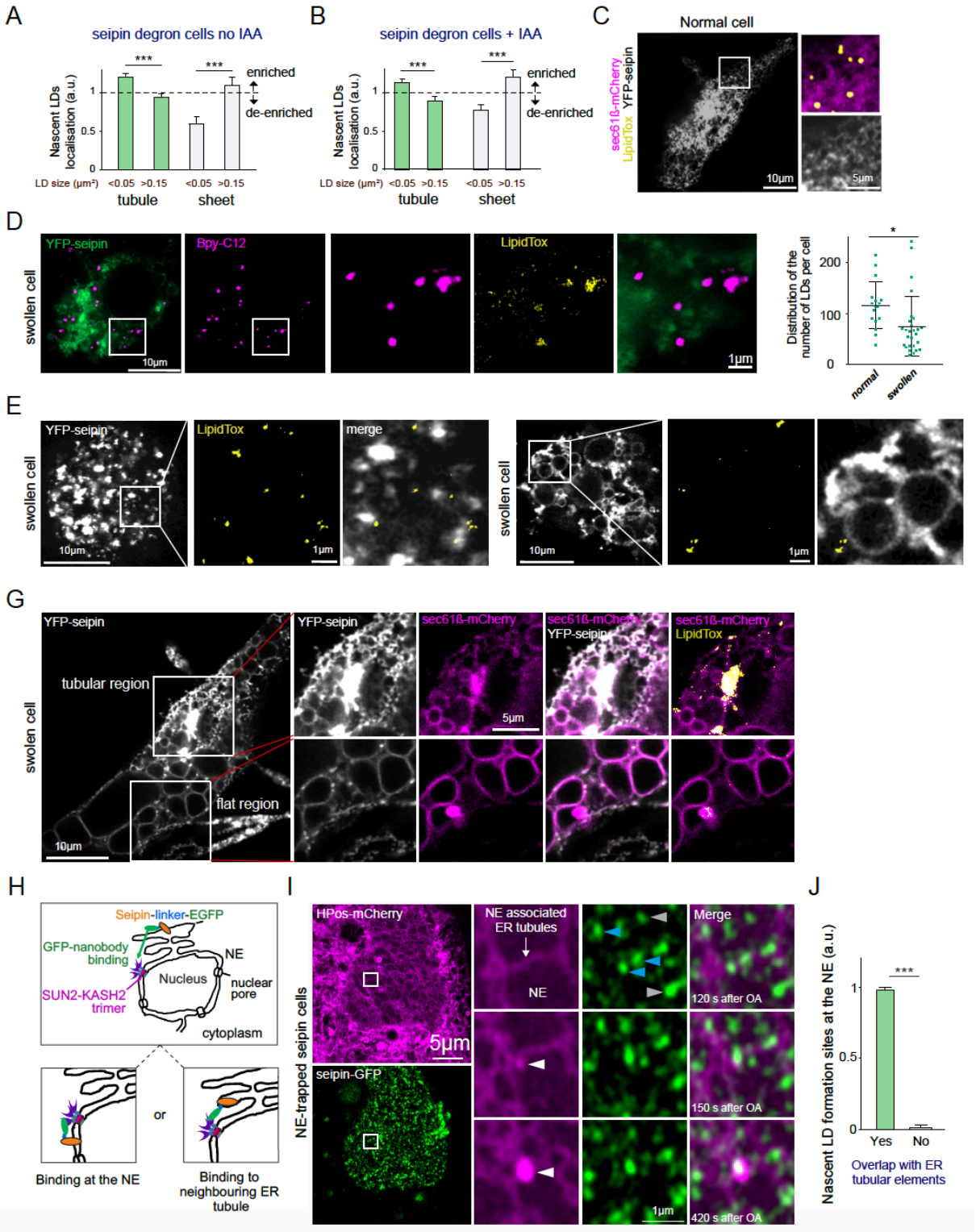

Figure S2. Related to figure 2

A-B) Additional analysis of the data in Figure 2 A-B. For each LD, the overlapping segmented ER pixels were compared to overall pixel distribution of sheets/tubules in the same cell. Smaller LDs are more enriched at ER tubules than larger LDs. Bars: mean +/- SEM, n= 80-256 LDs/group, 2 experiments.

C) Cos7 cells expressing YFP-seipin and sec61 were imaged 15 min after OA addition. Cells overexpressing seipin are able to generate LDs, stained by LipidTox.

D) Related to Figure 2C, Cos7 cells expressing YFP-seipin were imaged 20 min after ER-vesicle induction and OA and Bpy-C_{12} addition. LDs are also formed under this condition. Right: number of newly formed LDs in normal vs. swollen Cos7 cells, mean +/- SEM; n = 17 normal cells, n = 27 swollen cells, 3 experiments.

E) Cos7 cells expressing YFP-seipin were imaged 15 min after OA and Bpy-C_{12} addition (20 min after ER-vesicles formation). LDs have been formed near submicrometric seipin spots but not on large micrometric vesicles containing seipin.

F) Swollen Cos7 cells expressing YFP-seipin and sec61 were imaged 15 min after OA addition. Most forming LDs were localized on submicrometric membranes (z-stack 2).

G) Related to Figure 1K. A swollen Cos7 cell expressing YFP-seipin and sec61 and still harboring a conserved ER tubular region was imaged 15 min after OA addition. Most forming LDs are localized on tubular membranes.

H) Schematic of the seipin NE-trap, for trapping endogenously GFP-tagged seipin at the NE, originally described in (REF: SALO ET AL 2019)**.**

I) Stable seipin NE-trapped cells were delipidated (2 d LPDS, 18 h DGATi), transfected with HPOS-mCherry for the last 24 h and imaged live after OA administration. Gray arrowheads: seipin at the NE, blue arrowheads, seipin at NE-associated ER tubules, white arrowheads: a forming nascent LD.

J) Analysis of I, newly formed LDs were scored based on overlap with a nearby ER tubule at first appearance, mean +/- SEM, n= 9 cells (56 LDs), 2 experiments.

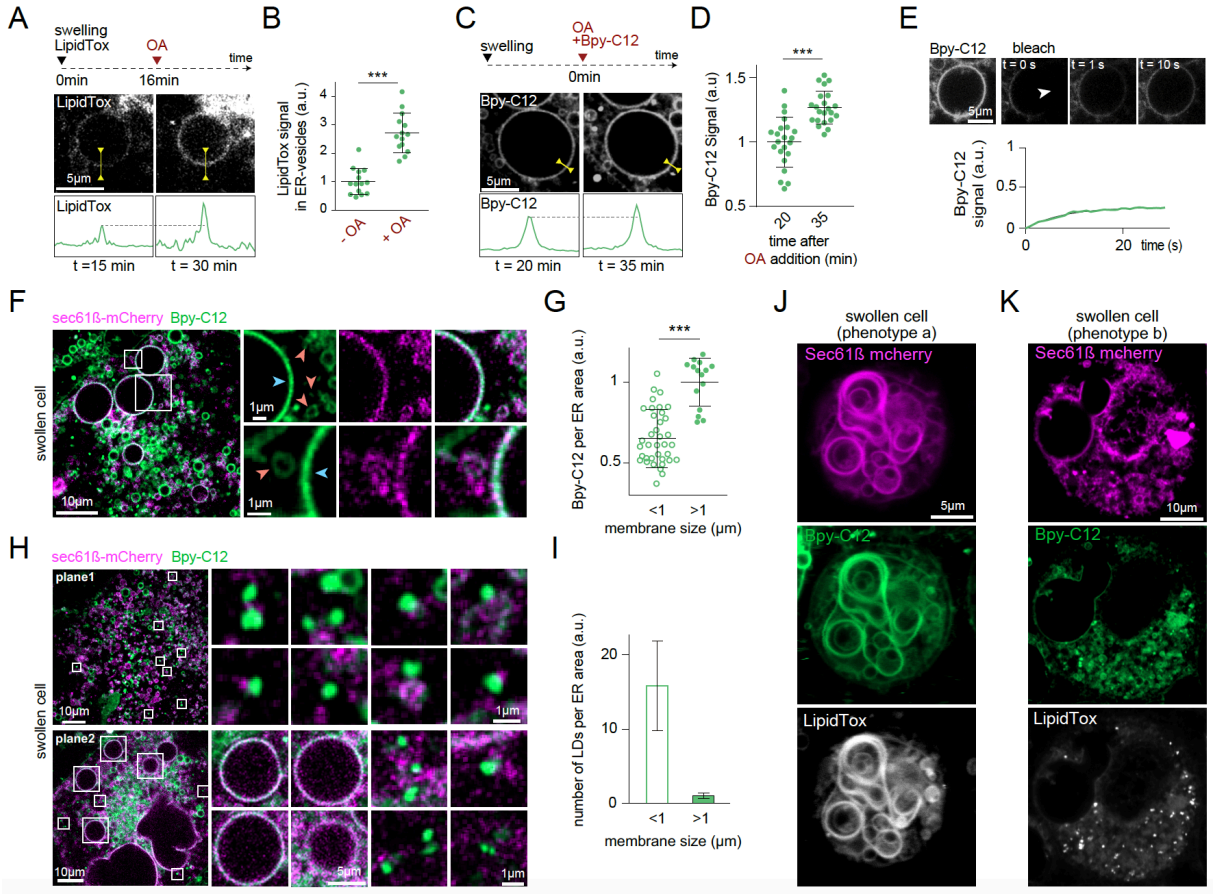

Figure 3: Neutral lipid and LD distribution in ER-vesicles.

A) ER-vesicles were induced in Cos7 cells in the presence of LipidTox and OA is added 15 min later. The LipidTox signal in an ER-vesicle before and 15 min after OA addition is shown, with the membrane intensity profile displayed below the images.

B) Analysis of A. Mean +/- SEM; n = 14 vesicles, 4 cells, 2 experiments.

C) Bpy-C_{12} signal in Cos7 cell ER-vesicles 20 min and 35 min after OA addition. Line scan shows an increase in signal.

D) Analysis of B. Mean +/- SEM; n = 22 vesicles, 5 cells, 2 experiments.

E) Rapid Bpy-C_{12} signal recovery in a partly bleached large ER-vesicle; arrowhead indicates the bleached area.

F) ER-vesicles induced in Cos7 cells expressing sec61ß-mCherry were imaged 15 min after OA and Bpy-C_{12} addition. Bpy-C_{12} signal intensity is higher in large micrometric-sized vesicles (blue arrowhead) than in submicrometric vesicles (red arrowhead).

G) Analysis of E), mean +/- SEM; n = 15-38 vesicles, 3 cells, 2 experiments.

H) ER-vesicles induced in Cos7 cells expressing sec61ß- mCherry were imaged 15 min after OA and Bpy-C_{12} addition. Two planes of a single cell are shown. Most forming LDs are localized on submicrometric membranes.

I) Analysis of H. Number of LDs per ER-vesicle size. Mean +/- SEM; n = 3268 LDs, 5 cells, 4 experiments.

J) A swollen Cos7 cell, expressing sec61ß-mCherry and imaged 30 min after OA and Bpy-C_{12} addition exhibits large onion ring-like ER membrane structures full of free NLs, reported by both Bpy-C_{12} and LipidTox.

K) Example of another cell treated as in J, that has formed submicrometric ER structures and was able to assemble LDs.

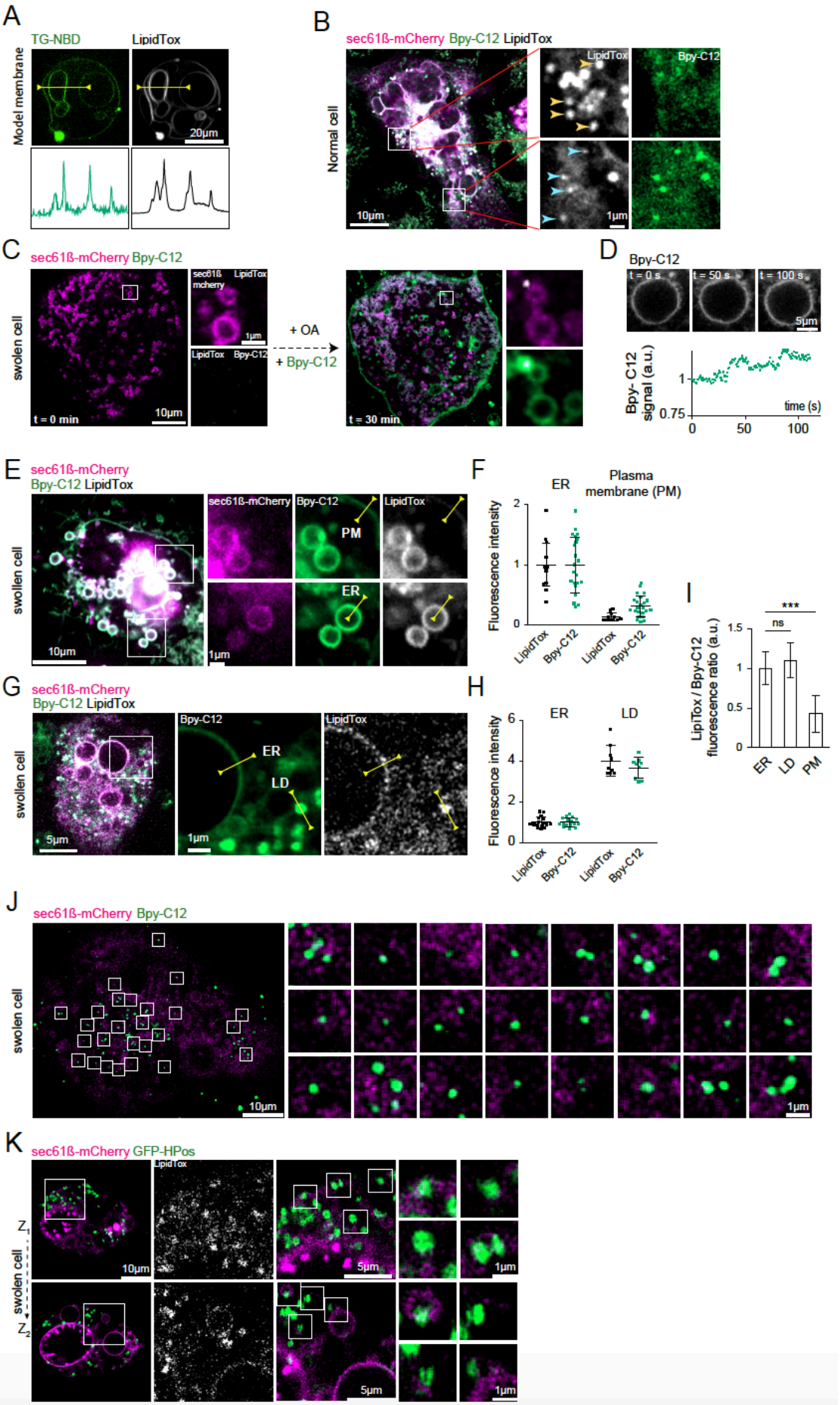
A
TG-NBD
LipidTox
Model membrane
20µm
B
sec61ß-mCherry Bpy-C12 LipidTox
Normal cell
LipidTox
Bpy-C12
10µm
1µm
C
sec61ß-mCherry Bpy-C12
swollen cell
sec61ß mcherry
LipidTox
LipidTox Bpy-C12
1µm
t = 0 min
10µm
+ OA
+ Bpy-C12
t = 30 min
D
Bpy-C12
t = 0 s
t = 50 s
t = 100 s
5µm
Bpy- C12 signal (a.u.)
1
0.75
time (s)
0
50
100
E
sec61ß-mCherry
Bpy-C12 LipidTox
swollen cell
sec61ß-mCherry
Bpy-C12
LipidTox
PM
ER
10µm
1µm
F
ER
Plasma membrane (PM)
Fluorescence intensity
2
1
0
LipidTox
Bpy-C12
LipidTox
Bpy-C12
I
***
ns
LipiTox / Bpy-C12 fluorescence ratio (a.u.)
1.5
1
0.5
0
ER
LD
PM
G
sec61ß-mCherry
Bpy-C12 LipidTox
swollen cell
Bpy-C12
LipidTox
ER
LD
5µm
1µm
H
ER
LD
Fluorescence intensity
6
4
2
0
LipidTox
Bpy-C12
LipidTox
Bpy-C12
J
sec61ß-mCherry Bpy-C12
swollen cell
10µm
1µm
K
sec61ß-mCherry GFP-HPos
LipidTox
swollen cell
Z1
Z2
10µm
5µm
1µm
5µm
1µm

Figure S3: related to figure 3

A) Model DOPC bilayer membranes were made and mixed with free TG, TG-NBD and LipidTox. LipidTox and TG-NBD signal intensity correlate with each other.

B) Normal Cos7 cells expressing sec61ß-mCherry were imaged 15 min after OA and Bpy-C_{12} addition. Newly formed LDs exhibit a colocalization (bottom panel) between LipidTox and Bpy-C_{12}, whilst pre-existing LDs (top panel) have less Bpy-C12 signal.

C) Time course of Cos7 cells expressing sec61ß-mchery, imaged 5 min after ER-vesicles formation before OA addition (left panel), and 15 min after OA and green Bpy-C_{12} addition. Bpy-C_{12} colocalizes with LipidTox at newly formed LDs. Note that in Figure 2, red Bpy-C_{12} was used.

D) ER-vesicles were induced in Cos7 cells and Bpy-C_{12} and OA was added to the cells. Analysis of Bpy-C_{12} signal over time on an exemplary ER-vesicle**.**

E) Swollen Cos7 cells expressing sec61ß-mCherry were imaged 15 min after OA and Bpy-C_{12} addition. The Bpy-C_{12} and LipidTox signal intensity in the plasma membrane is lower than in ER-vesicles.

F) Analysis of E. Mean +/- SEM; n = 11 for LipidTox signal, n = 23 for Bpy-C_{12} signal, from 5 cells, 3 experiments.

G) Swollen Cos7 cells expressing sec61ß-mCherry were imaged 15 min after OA and Bpy-C_{12} addition. Bpy-C_{12} and LipidTox signals are detected in formed LDs and ER-vesicles.

H) Analysis of G. Mean +/- SEM; n = 16 ER-vesicles and 9 LDs from 2 cells, 2 experiments.

I) Additional analysis of E-H. The fluorescence intensity ratio of LipidTox and Bpy-C_{12} are represented for ER-vesicles, LDs and the plasma membrane. This ratio is the same for ER-vesicles and LDs (which contain NLs) but not for the plasma membranes (which lacks NLs). These data support that Bpy-C_{12} signal in ER-vesicles is very likely neutral lipids.

J) Cells were treated as in Figure 2H, additional examples of most forming LDs localizing on submicrometric membranes.

K) Swollen Cos7 cells expressing HPos-GFP and sec61ß- mCherry were imaged 15 min after OA and Bpy-C_{12} addition. Most forming LDs are localized on submicrometric membranes.

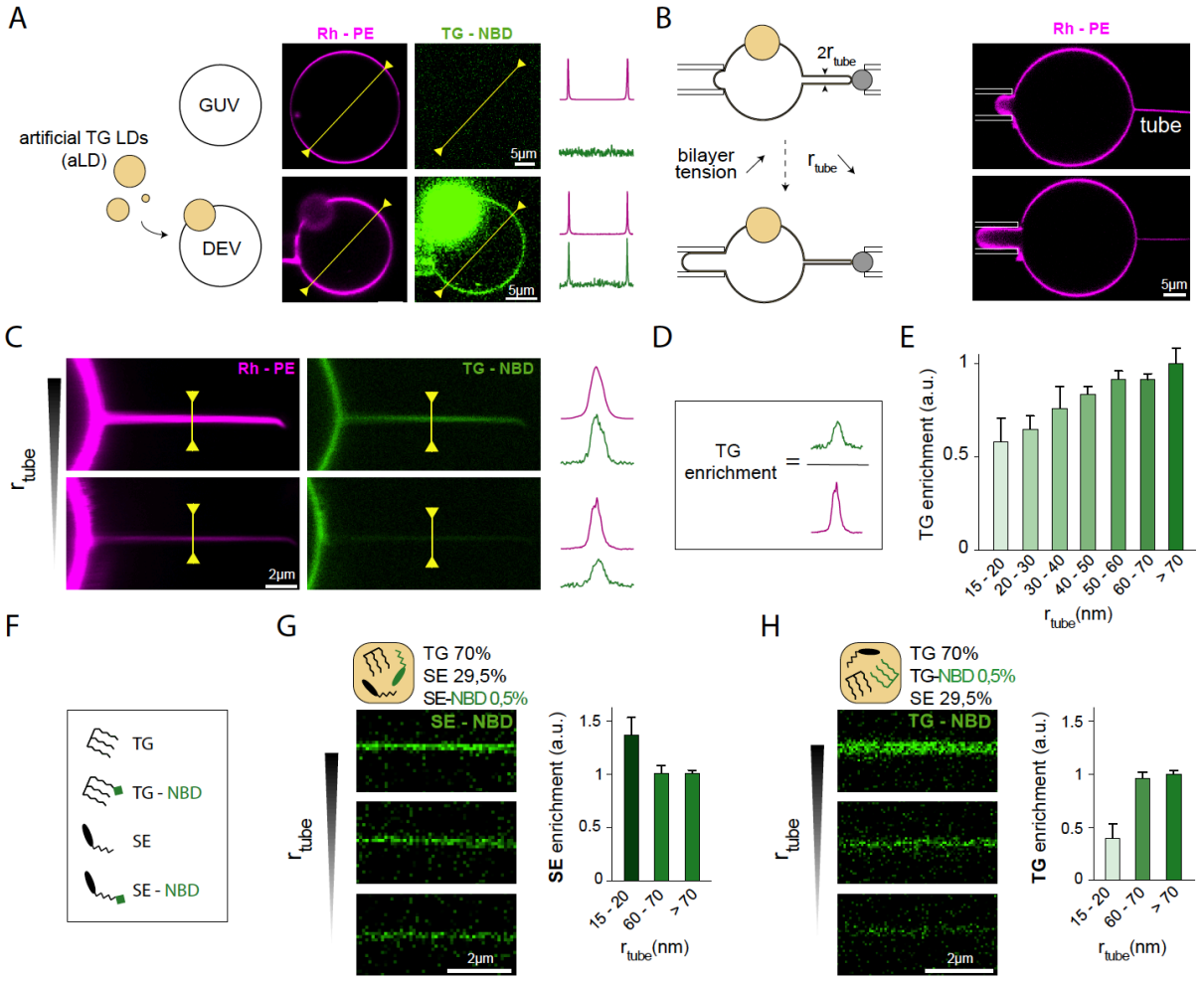

Figure 4. The presence of TG but not SE is unfavorable in tubules

A) Illustration of the DEV system consisting of GUVs mixed with aLDs. An exemplary DEV is shown. Rh-PE marks the membranes; TG-NBD marks the TG phase. The signal at the line scans (yellow lines) is shown.

B) A nanotube is pulled from a DEV by using streptavidin coated micro-beads bound to biotinylated phospholipids on the DEV. Increasing the bilayer tension with a micropipette decreases the tube radius.

C) Nanotubes with 60 nm and 20 nm diameters are pulled from a DEV. Line scans on the tubes indicate that TG-NBD signal intensity is reduced relative to Rh-PE signal as the tube radius is decreased.

D) Definition of the TG enrichment index in the tube.

E) Analysis of C. Plot of TG enrichment relative to the nanotube radius, rt_{ube}.

F) Schematic description of different oil molecules used in G and H. The green squares represent NBD.

G) Nanotubes are pulled from DEVs as in C, but the DEVs are made with aLDs containing TG, SE and SE-NBD as indicated (w/w). Analysis of the SE signal relative to tube radius is shown.

H) Same experiment as in G but with TG-NBD as indicated (w/w). Analysis of the TG signal relative to tube radius is shown.

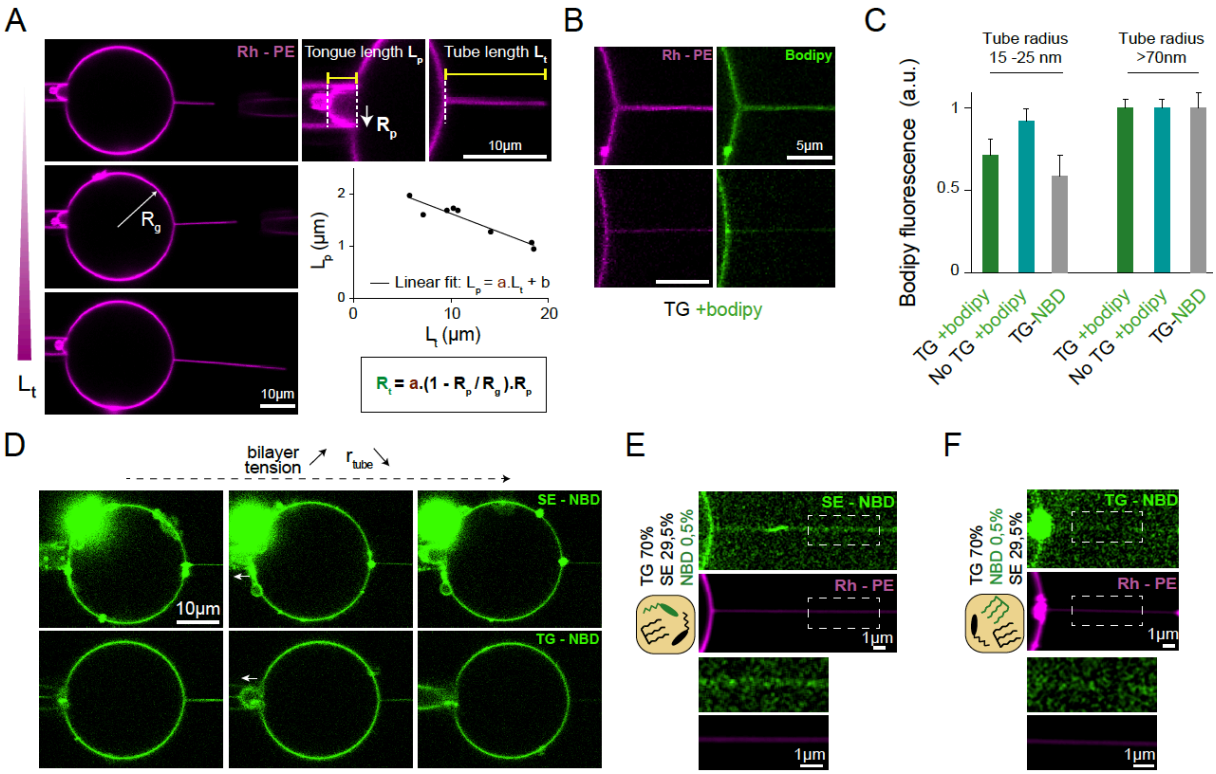

Figure S4: related to figure 4

A) Steps for the calibration of the nanotube radius based on Rh-PE fluorescence intensity (see Materials and methods). Increasing the tube length provokes a decrease in the tongue length due to surface area conservation. The tongue length relative to the tube length is plotted and fitted by a linear curve with a slope "*a*". This slope gives the nanotube radius.

B) Same experiments as in Figure 4C-E but with having TG only stained by Bodipy which was added to the medium.

C) Analysis of E based on Bodipy fluorescence normalized to Rh-PE. Signal on the tube is represented relative to the tube radius. Same trend is observed as in Figure 4E. A control is shown without the presence of TG and having only Bodipy. Bars: mean +/- SEM.

D) Visualization of the entire GUV membrane showing the distribution of SE-NBD or TG-NBD in response to reducing the tube radius. The tongue in the micropipette is aspirated to decrease the nanotube radius.

E) Same experiments as in Figure 4C with Rh-PE and SE-NBD signals for a radius of 20 nm.

F) Same experiments as in Figure 4C, with Rh-PE and TG-NBD signal for a radius of 20 nm.

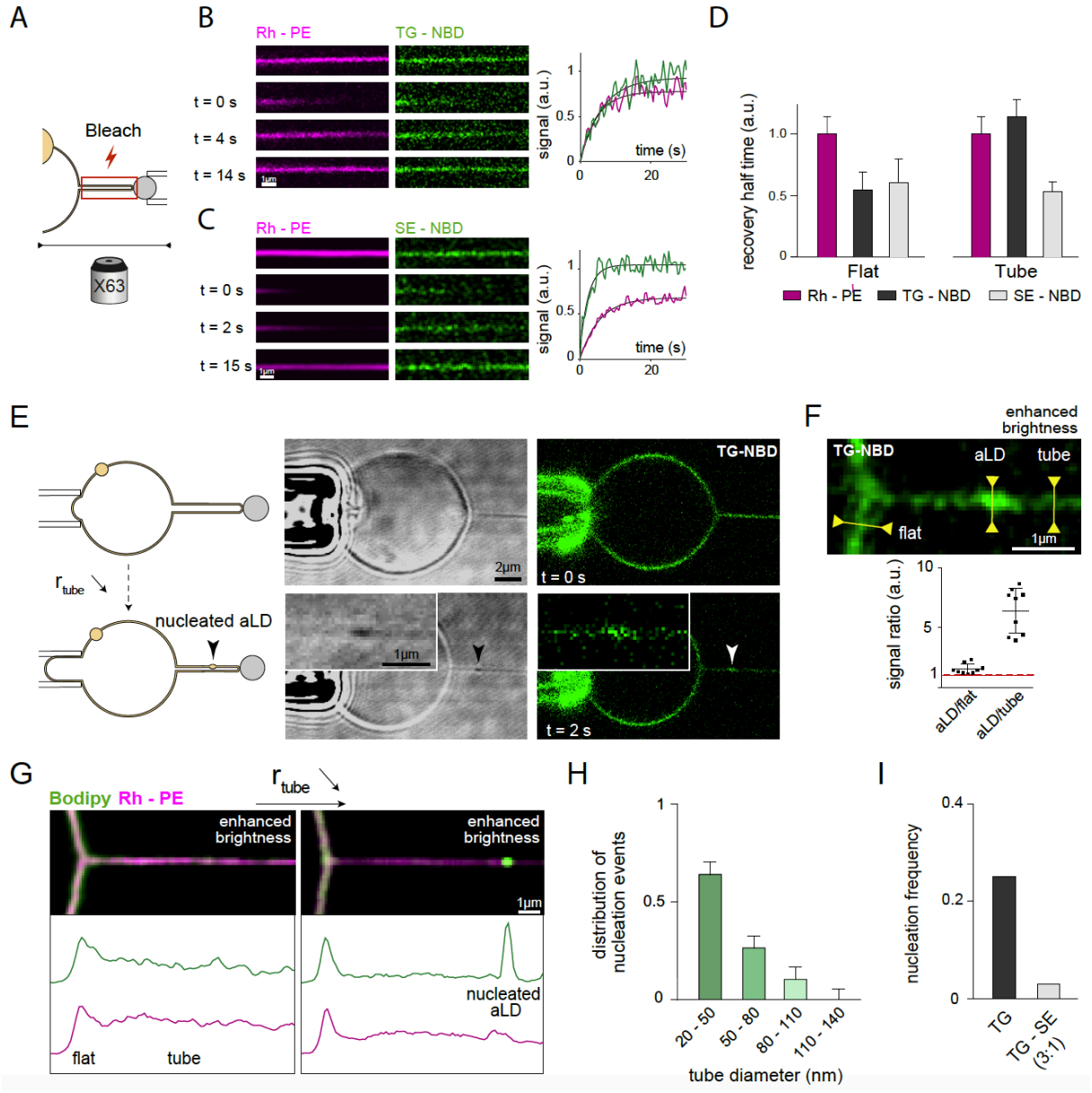

Figure 5. Membrane curvature more efficiently triggers the assembly of *in vitro* TG than SE LDs

A) Diagram of the FRAP region where both Rh – PE and TG –NBD or SE – NBD are bleached in the entire nanotube.

B) Time sequence of Rh-PE and TG-NBD recovery following photobleaching. The normalized fluorescence intensity evolution of the bleach region is shown with its fitting curve. Experiment was repeated three times.

C) Time sequence of Rh-PE and SE-NBD recovery following photobleaching. The normalized fluorescence intensity evolution of the bleach region is shown with its fitting curve. Experiment was repeated three times.

D) Analysis of B and C. Plot of the average recovery half time of Rh-PE, TG-NBD and SE-NBD (normalized by Rh – PE) as a function of membrane curvature. For examples of photobleaching recovery in flat membranes, see Figure S5.

E) A nanotube is pulled from a DEV by using streptavidin coated micro-bead. Submitting the bilayer to a sudden increase of surface tension causes a drastic increase in curvature. An artificial TG LD is nucleated following this manipulation. The arrowhead shows the nucleated TG aLD shown in the inset.

F) Smoothened image of the nucleated aLD from the inset in E is shown. For analysis of signal ratio, the intensity of the nucleated aLD signal is divided by the tube or the GUV intensity prior to nucleation. Bars: mean +/- SEM, n = 9.

G) An additional example of a nucleation event in a nanotube is shown with using TG only, labelled by Bodipy which was added to the medium. Signal profiles along the tube of Rh-PE and Bodipy are shown before and after nucleation.

H) Distribution of the nucleation events is reported against the final nanotube radius. Bars: mean +/- measurement uncertainty, n = 9.

I) Frequency of nucleation events observed relative to aLD NL composition. For TG, n = 9 nucleation events out of 36 trials; for TG-SE, n = 1 nucleation event out of 19 trials.

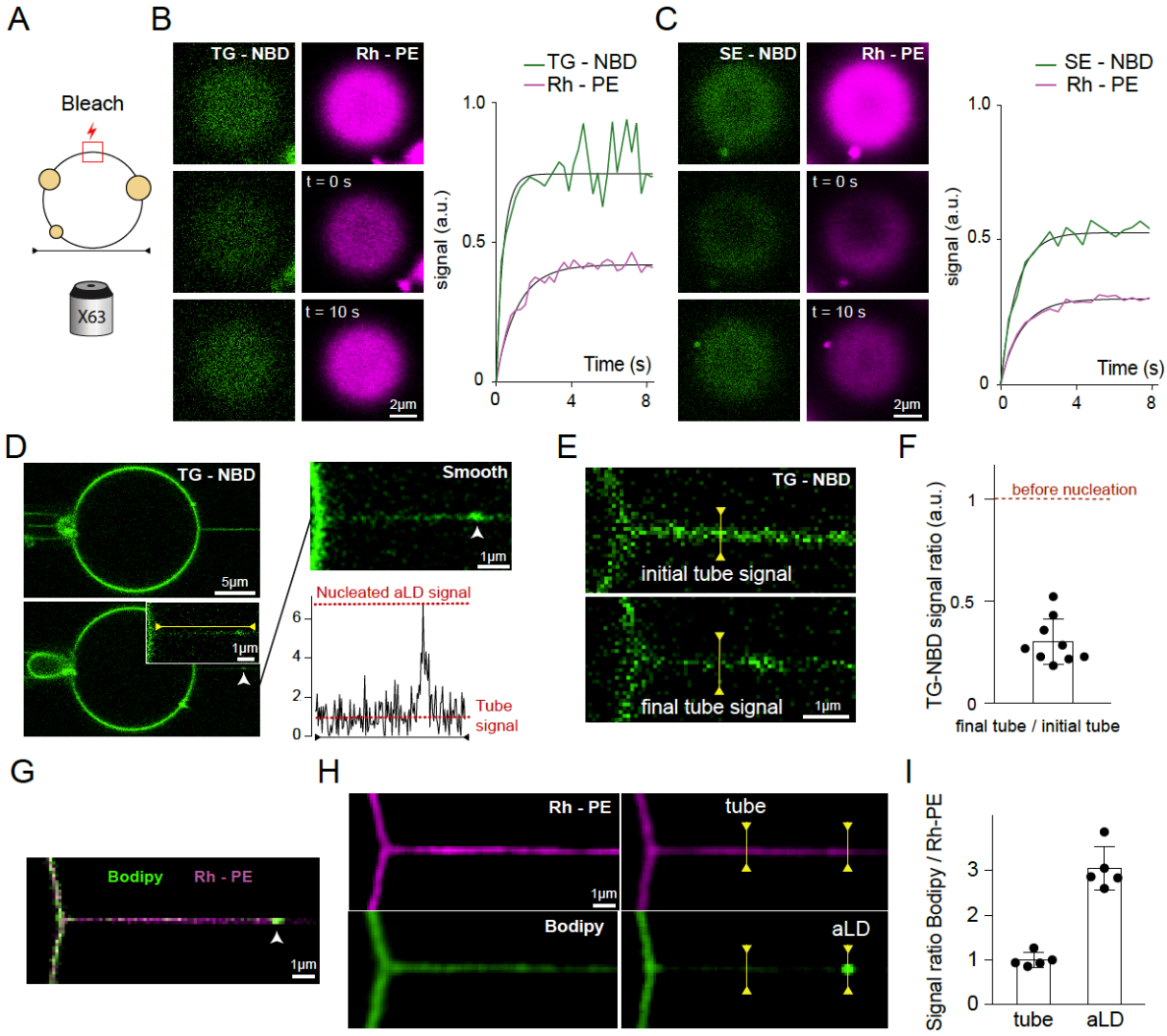

Figure S5: related to figure 5

A) Schematic representation of the FRAP experiment performed on planar regions at the apex of the DEV. Both Rh-PE and TG-NBD or SE-NBD are bleached.

B) FRAP experiment as in A, performed on a DEV made with TG-NBD. Shown is the normalized recovery profiles and fitted curves. The experiment was repeated three times.

C) FRAP experiment as in A, performed on a DEV made with SE-NBD. Shown is the normalized recovery profiles and fitted curves. The experiment was repeated three times.

D) An additional example of a nucleation event is shown.

E) Zoom on the nucleation event in Figure 5E, before and after nucleation of the aLD. The TG-NBD signal in the tube outside of the nucleated aLD decreases after the reduction of the tube radius.

F) Analysis of E. The TG-NBD signal ratio in the tube before and after nucleation. Bar: mean +/- SEM, n = 9 nucleated aLDs.

G) Merge of Rh-PE and Bodipy channels of Fig 2G and S2G is shown (not smoothened).

H) Rh-PE and Bodipy channels of Figure 5G are shown separately (smoothened).

I) Analysis of Figure 5G showing the signal intensity ratio of Bodipy relative to Rh-PE in the tube and the nucleated aLD. Bars: mean +/- SEM, n = 5.

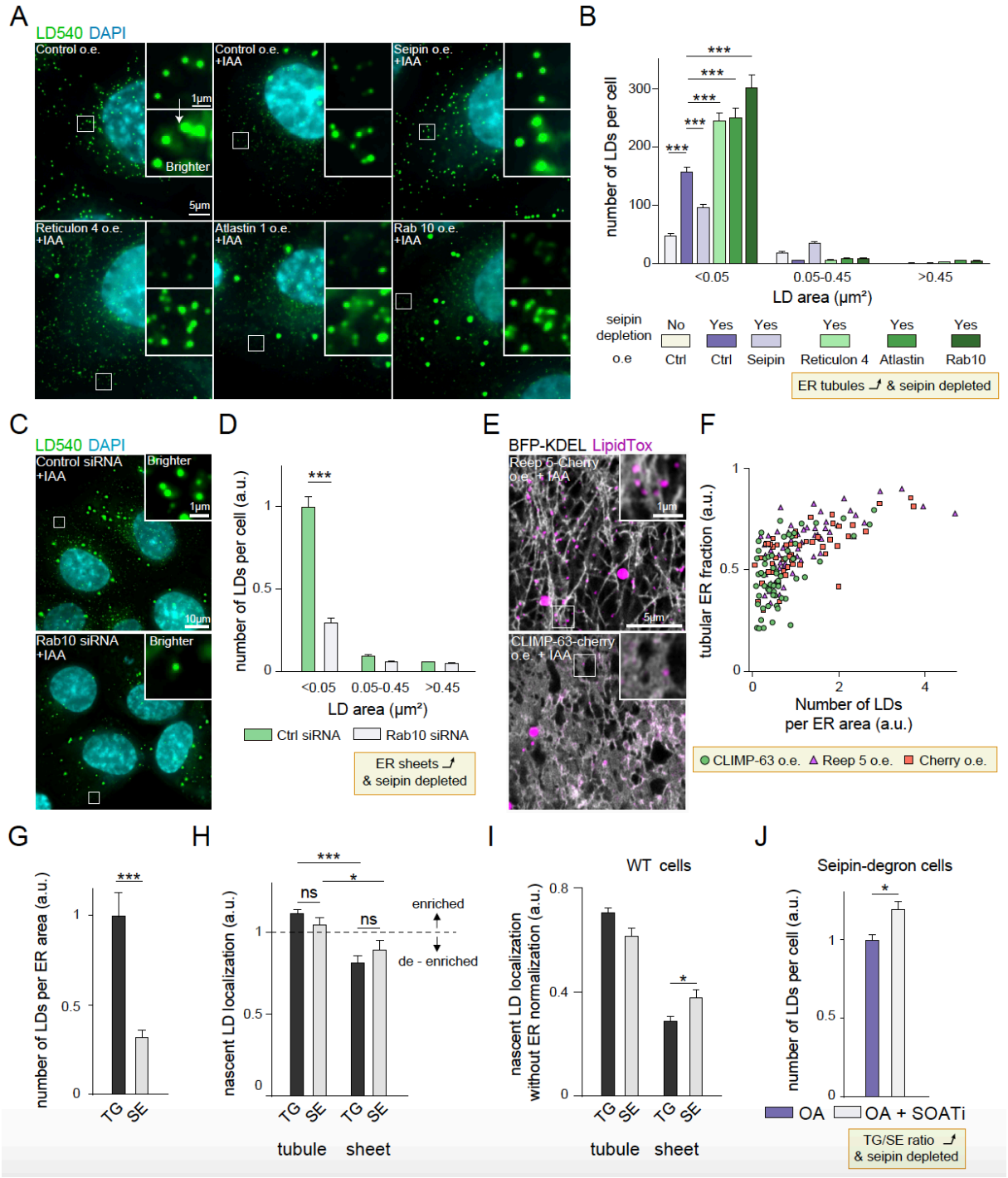

Figure 6. Modulation of sheet/tubule ratio alters LD assembly

A) ER tubule proteins were stably overexpressed in seipin degron cells. Cells were delipidated for 3 d, seipin was depleted by IAA treatment for 18 h and LD biogenesis was induced by OA 1 h treatment. Cells were fixed, stained with LD540 and DAPI and imaged by widefield microscopy. Maximum intensity projections of deconvolved z-stacks.

B) Analysis of A. Bars: mean +/- SEM, n = 167-549 cells/group, 2 experiments.

C) Seipin degron cells were treated with control or Rab18 siRNA for 3 d in LPDS including 18 h IAA treatment to deplete seipin. Cells were then treated with OA for 1 h, fixed and stained as in A.

D) Analysis of C. Bars: mean +/- SEM, n = 344-353 cells/group, 2 experiments.

E) Seipin degron cells stably expressing BFP-KDEL were transfected with indicated plasmids for 2 d, including 1 d delipidation (LPDS, DGATi) and IAA treatment. After DGATi washout, cells were imaged live with Airyscan microscopy starting 45-75 min after OA addition in the presence of LipidTox Green.

F) Analysis of E. Peripheral ER ROIs were segmented for sheets and tubules using the BFP-KDEL channel and the number of LDs plotted (normalized to total ER area in each ROI) relative to ER morphology, n = 138 ROIS from 138 cells, 2 experiments.

G-I) Cells were treated imaged and analyzed as in Figure 1D-E. Bars: mean +/- SEM, n = 39 cells/group, 3 experiments (428-1095 LD-associated seipins). The data for TG LDs is same as in Figure 1E WT LDs. In H**,** the distribution of segmented ER pixels at LD-associated seipin foci was compared to the overall pixel distribution of sheets/tubules in the same cells, in I the distribution of segmented ER pixels at LD-associated seipin foci is shown without normalization to overall ER pixel distribution.

J) Seipin degron cells were delipidated for 3 d (including 18 h with DGATi) and treated with OA with or without SOAT1 inhibitor for 1 h, fixed, stained and analyzed for LD sizes as in A. Bars: mean +/- SEM, n = 308-368 cells/group, 2 experiments.

The insets in A and C show tiny LDs, brightness is adjusted to display them more clearly.

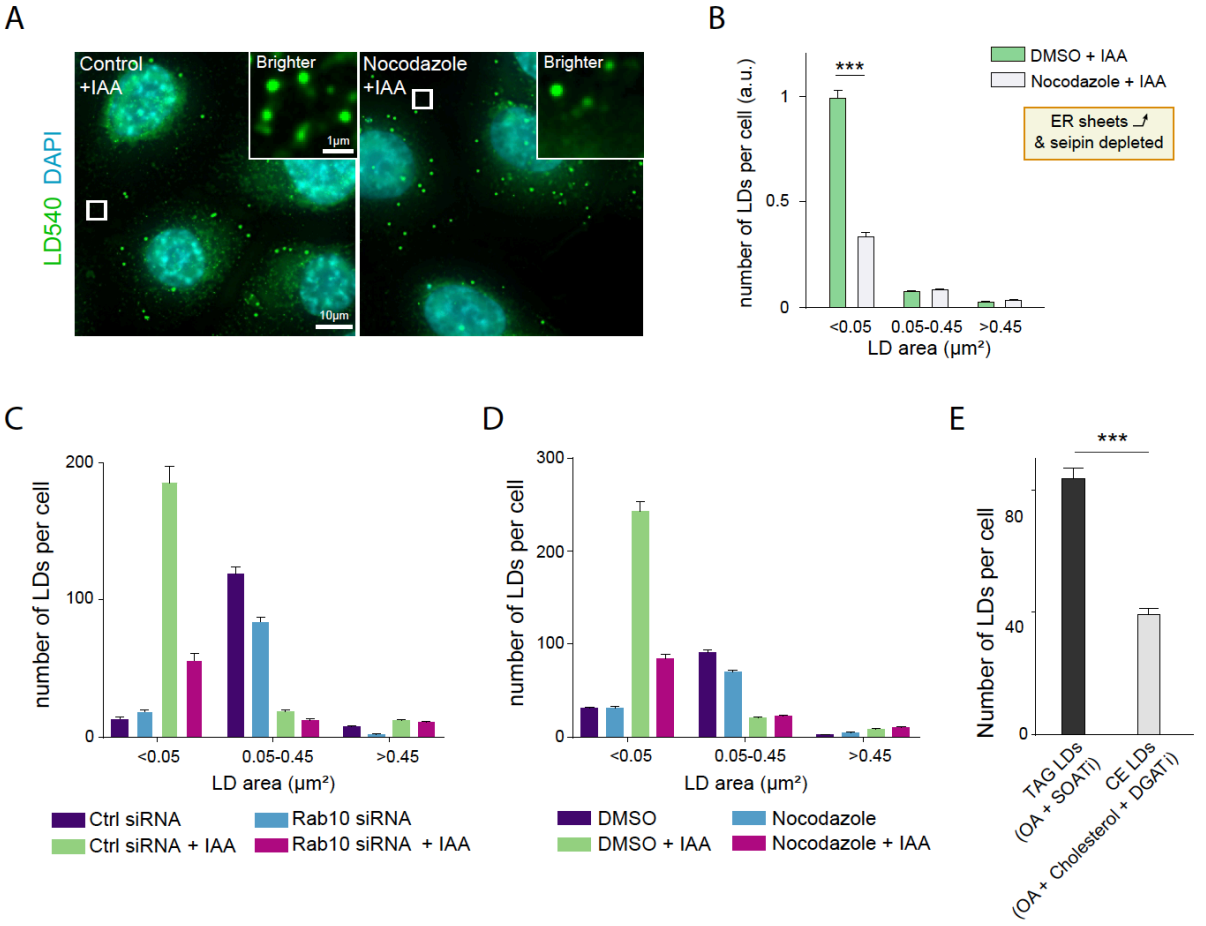

Figure S6: related to figure 6

A) Seipin degron cells were delipidated for 3 d, including 18 h IAA treatment to deplete seipin. Cells were then treated with DMSO or nocodazole for 15 min prior and during 1 h OA loading, fixed, stained and imaged as in Figure 6A.

B) Analysis of A. Bars: mean +/- SEM, n = 487-584 cells, 3 experiments.

C) Seipin degron cells were treated with control or Rab18 siRNA for 3 d in LPDS +/- 18 h IAA to deplete seipin. Cells were then treated with OA for 1h, fixed and stained as in Figure 6A. Bars: mean +/- SEM, n = 293-353 cells/group, 2 experiments.

D) Seipin degron cells were delipidated for 3 d +/- 18 h IAA to deplete seipin. Cells were then treated with DMSO or nocodazole for 15 min prior to and during 1 h OA loading, fixed, and imaged as in Figure 6A. Bars: mean +/- SEM, 487-656 cells/group, 3 experiments.

E) A431 WT cells were delipidated (3 d LPDS, 18 h DGATi) and treated with 200 µM OA and SOAT1 inhibitor, or 200 µM OA, 200 µM cholesterol and DGATi for 30 min. Cells were then fixed and stained as in Figure 6A. Bars: mean +/- SEM, n = 330-352 cells/group, 2 experiments.

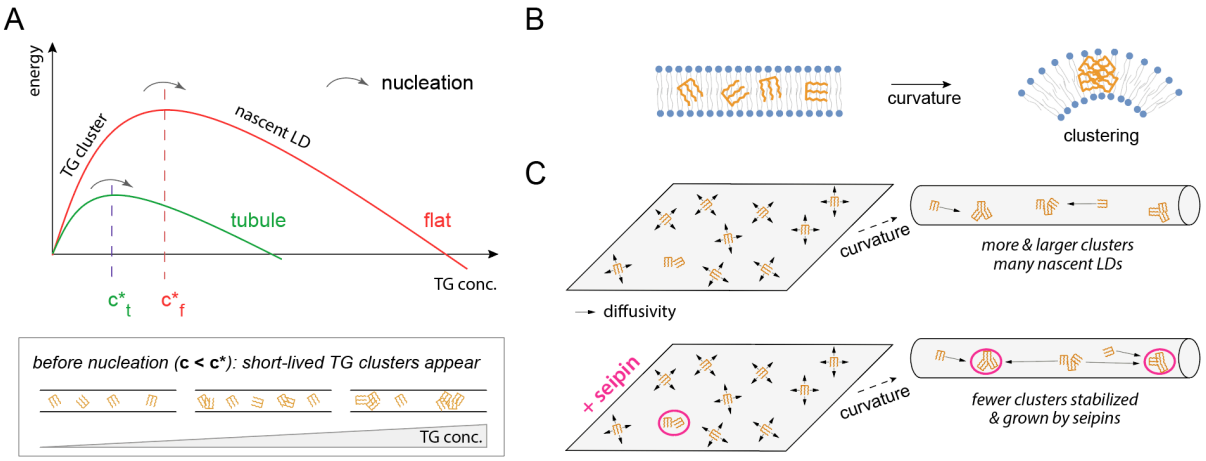

Figure 7. Model for the role of curvature and seipin in triggering LD assembly

A) (top) Illustration of the energy profile of phase transitions in the context of LD assembly. Curvature decreases the critical concentration and the energy barrier for nucleation. (Bottom) nomenclature used. Before the critical nucleation concentration, c*, short-lived TG clusters appear (msec). Above this concentration, nascent droplets form.

B) Proposed mechanism by which curvature favors TG clustering, by exposing the hydrophobic core to water molecules.

C) Without seipin, many TG clusters are triggered at tubules and transit into nascent droplets. (bottom) Seipin stabilizes clusters in tubules, TGs favorably move to these seipin-stabilized clusters, which will turn into nascent LDs, fewer in number than without seipin.

Materials and methods

Reagents

Mouse anti-Xpress (Thermo Fisher R910-25, IF 1:500); Alexa 647 anti-mouse (Thermo Fisher A-31571, IF 1 :400); LD540 (Spandl et al., 2009) (synthesized by Princeton BioMolecular Research, fixed cells 0.1 µg/ml, live cells 0.03-0.05 µg/ml); DAPI (Sigma D9542, 10µg/ml); Prolong Live Anti-Fade (Thermo Fisher P36975, live cells 1:100); Lipofectamine LTX and Plus Reagent (Thermo Fisher, 15338100); Hiperfect (Qiagen, 301705); X-tremeGENE™ 9 DNA Transfection Reagent was from Roche; Fetal bovine serum (FBS) and penicillin-streptomycin (PS) were from Life Technologies; DGAT1 inhibitor (Sigma PZ0207, 5 µM); DGAT2 inhibitor (Sigma PZ0233, 5 µM); SOAT inhibitor (Sandoz 058-035nSigma, 2 µg/ml); Indole-3-acetic acid sodium (IAA, Santa Cruz sc-215171, stock dissolved in mqH20, final concentration used 500 µM); Cell-SIR647 (New England Biolabs, S9102S, stock dissolved in DMSO, final concentration used 0.3 µM); Geneticin (G418) sulphate (Gibco, 11811-031, 0.6 mg/ml-A431); Zeocin (Invitrogen, R250-01; 0.2 mg/ml); human fibronectin (Roche Diagnostics, 11051407001);), 8-well Lab-Tek II #1.5 coverglass slides (Thermo Fisher, 155409), #1.5 polymer µ-slide 8 well ibiTreat chambers (Ibidi, 80826), formaldehyde (Sigma P-6148), nocodazole (M1404-2MG, dissolved in DMSO, final concentration used 20 µM). Bodipy 493/503, Bodipy-C_{12} 500-510, and Bodipy-C_{12} 558-568 were from Thermo Fisher Scientific. Oleic acid was from Sigma Aldrich; DOPC (1,2-dioleyl-sn-3glycero-3-phosphocholine), biotynil-DOPE (1,2-dioleyl-sn-glycero-3-phosphoetanolamine-N-(biotinyl)) and Rhodamine-DOPE (1,2-dioleyl-sn-glycero-3-phophoethanolamine-N-(lissamine rhodamine B sulfonyl) were from Avanti Polar Lipids; Chloroform was from Sigma Aldrich. Triolein was from Sigma Aldrich and TG-NBD (1,3-Di(cis-9-octadecenoyl-2-((6-(7-notrobenz-2-oxa-1, 3-diazol-4-yl) amino) hexanoyl) glycerol was from Setareh biotech. Cholesteryl oleate was from Sigma Aldrich. SE-NBD (5-cholesten-3β-ol 12-[(7-nitro-2-1,3-benzoxadiazol-4-yl)amino]dodecanoate) was from Avanti polar lipids. Streptavidin coated microspheres were from Bangs Laboratories. Glass coverslips were from Menzel Glaser were from Braunschweig, Germany. 35 mm coverslip dishes were from MatteK ref P35G-0-20-C. Capillaries for micropipette (1.0oDx0.58iDx150Lmm 30-0017 GC100-15b) were from Harvard Apparatus. Other reagents, including cell culture reagents and solvents, were from Gibco/Thermo Fisher, Lonza and Sigma, Merck and Honeywell

Cell culture

A431 cells (ATCC CRL-1555, sex: female) were maintained in Dulbecco's modified Eagle's medium (DMEM) containing 10% fetal bovine serum (FBS), penicillin/streptomycin (100 U/ml each), L-glutamine (2 mM) at 37°C in 5% CO_2. Cos7 and HeLa cells were maintained in DMEM supplemented with 10% heat inactivated FBS and 1% penicillin-streptomycin. Cos7 and HeLa

cells were cultured in 35 mm coverslip dishes (MatteK ref P35G-0-20-C) 16 h at 37°C under a 5% CO2 atmosphere prior to transfection. Transfections of plasmids (Lipofectamine LTX with PLUS Reagent and X-tremeGENE™ 9 DNA Transfection Reagent) and siRNAs (HiPerfect) were carried out according to the manufacturer's instructions. Cells were incubated for 24 h and then imaged, or subjected to feeding or swelling experiment (detailed below). For feeding control experiments, cells were fed with oleic acid (Sigma Aldrich) at 400 µM conjugated to 1% bovine serum albumin solution (BSA) in DMEM during 15 minutes at 37°C to promote LDs formation.

siRNAs and plasmids

Reticulon 4 (NM_207520.1), RAB 10 (NM_016131.4) and Atlastin 1 (NM_001127713.1) cDNAs were amplified from A431 cDNA and inserted into pcDNA4/HisMaxC vector through restriction ligation. Seipin (BC012140) cDNA was amplified by PCR from a plasmid kindly provided by Hongyuan Yang (Fei et al., 2008b), and inserted into pcDNA4/HisMaxB. CLIMP63 (NM_006825.3 with nucleotide 210-212 deletion) was amplified from A431 cDNA and inserted into pmCherry-C1 through restriction cloning. REEP5 (NM_005669.5) was amplified from A431 cDNA and inserted into pEGFP-N1 or pmCherry-N1 vector through restriction cloning. Primer sequences are available upon request. BFP-KDEL cDNA (Addgene #49150) was a gift from Gia Voeltz (Friedman et al., 2011). HPos-mCherry has been described (Salo et al., 2016). Ctrl siRNA has been described (Hölttä-Vuori et al., 2013). Pre-validated siRNA against Rab10 was from Qiagen (#1027415, target sequence: ACTGCGTCCTTTTTCGTTTT). YFP-Seipin was a gift from Dr. Mathias Beller; sec61ß-mCherry was purchased from Addgene (#49155) and was from the group of Gia Voeltz (Zurek et al., 2011); pEGFP-HPos was a gift form Dr. Albert Pol (Kassan et al., 2013).

Stable cell lines

A431 end-miniIAA7-GFP-Sec61β cells have been described (Li et al., 2019), these harbor end-miniIAA7-GFP tag at the endogenous locus of Sec61β. A431 seipin degron cells, seipin NE-trapped cells, Rab18 KO cells, end-seipin-sfGFPx7 cells expressing BFP-KDEL and LiveDrop-mCherry and end-seipin-SNAPf cells have been described (Salo et al., 2019). Seipin-degron-A cells were used for data in Figures 2A, 6A-B, 6E-F, 6J, S6A-B. Seipin-degron-B cells were used for the data in Figures 6C-D. To generate stable cells expressing the ER luminal marker BFP-KDEL, cells were transfected with BFP-KDEL cDNA and single clones were obtained as described in (Salo et al., 2019). To generate stable pools overexpressing seipin, reticulon 4, atlastin 1 and Rab10, seipin-degron A cells were transfected with the respective plasmids and the expressing cell populations enriched using zeocin, pcDNA4/HisMax C alone was used as a control plasmid. Experiments were conducted 2-3 weeks after selection.

Large ER-derived Intra-Cellular vesicle experiments

For swelling experiments, Cos7 and HeLa cells were first transfected for 24 h with the indicated plasmids. The culture media of the cells was next replaced by a hypotonic culture media (DMEM:H2O 1:20). The cells were then incubated at 37°C, 5% CO2 for 5 minutes, to induce ER-vesicles. For analyzing seipin localization (Figures 1J-L and S1A-C), cells were imaged directly after swelling. For Figures 2C-I, 3, S2C-H and S3 the cells were next incubated with 400 µM OA conjugated to 1% (w/w) BSA in DMEM:H2O (1:20) media at 37°C to induce LDs formation. For Figures 2C-D and S2D, Bpy-C_{12} 558/568 was also added to OA (1:1000) to stain nascent LDs. Z-stacks imaging of entire cells were done before and 15 min after OA administration. For Figures 3 and S3A-B, Bpy-C_{12} 500/510 was added to OA (1:1000) to induce and visualize nascent LDs and TG localization. Z-stacks of the entire cell were imaged after swelling, before feeding, and 15 minutes after feeding. For Figure S3C, GFP-HPos is used as a marker for LDs. In all experiments where LipidTox deep red was used, it was always added in the swelling medium, before OA addition, to mark pre-existing and emerging nascent LDs, and also ER-vesicles hydrophobicity.

Delipidation, DGATi Treatments, LD Induction, seipin depletion with IAA, SNAP-labeling

Where indicated, cells were delipidated by culturing in serum-free medium supplemented with 5% lipoprotein deficient serum (LPDS). LPDS was prepared as described in (Goldstein et al., 1983). Where indicated, cells were additionally incubated with DGAT1 and DGAT2 inhibitors for the final 18 h, DGATi indicates treatment with both inhibitors. To wash out DGATi, cells were washed three times with PBS and incubated in 5% LPDS medium for 5 min prior to inducing LD biogenesis with 0.2 mM OA or 0.2 mM cholesterol-cyclodextrin (final concentration) for indicated times. OA complex with BSA in 8:1 molar ratio was prepared in serum-free DMEM or FluoroBrite DMEM as described (Hölttä-Vuori et al., 2013) and 2.5 mM stock of cholesterol/methyl-b-cyclodextrin complex was prepared as described (REF: SANDHU ET AL CELL). For depletion of seipin, IAA was added to the medium for 18 h, vehicle control was Milli-Q-H_2O (1:100).

Live cell analysis of LD formation sites and ER morphology

Cells were seeded onto fibronectin-coated (10 mg/ml fibronectin for 1-2 h followed by washes in PBS) 8-well Lab-Tek II #1.5 coverglass slides. Imaging was performed in Fluorobrite DMEM medium supplemented with 5% LPDS. Live cell imaging was performed with Zeiss LSM 880 confocal microscope equipped with Airyscan (Fast) detector using a 63 X Plan-Apochromat oil objective, NA 1.4, at 37 ^{o}C, 5% CO_2 with incubator insert PM S1 and definite focus hardware

autofocus system. Imaging was done using Airyscan super resolution ILEX-mode (Figure 1A, 1F) or super resolution fast mode (Figure 1D, 2A), with sequential excitation of fluorophores using appropriate lasers and stable emission filter sets. The Airyscan detector was adjusted regularly between acquisitions and images were Airyscan-processed using default settings with the Zeiss Zen software package. For live cell time-lapse acquisitions, single focal planes were imaged with Airyscan fast mode, with frame rates of 650 ms (Figure 1A) or 110 ms (Figure 1F).

For analysis of nascent LD localization after LD formation (Fig 1D-E, 2A, 6E-H), cells were imaged as described above, imaging peripheral regions of the ER. The ER, LDs and seipins were segmented using ilastik and for each cell, the distribution of segmented ER pixels (either sheet or tubule) at either LD-associated seipins (Fig 1D-E, 6H-I) or at LDs (Fig 2A-B) was compared to the overall ER pixel distribution in the same cell, using CellProfiler and custom-made MATLAB scripts described in (Salo et al., 2019). From these data, the localization of seipins in the ER was also analyzed in a similar manner, comparing the distribution of segmented ER pixels at seipin foci to the overall ER pixel distribution in the same cell (Fig 1G).

For analysis of ER marker protein distribution, peripheral regions of the ER were imaged as described above. ER was segmented using the BFP-KDEL channel. The mean intensity ratio of BFP-KDEL at sheets vs tubules was analyzed and compared to the mean intensity ratio of ER marker proteins (REEP-5, CLIMP-63, SEC61ß) in that cell, using CellProfiler and custom-made MATLAB scripts described in (Salo et al., 2019).

LD analysis of fixed cells

Cells were seeded onto Ibidi µ-slide 8 well ibiTreat chambers. After indicated treatments, cells were washed with PBS, fixed with 4% PFA in 250 mM Hepes, pH 7.4, 100 mM$CaCl_2$ and 100 mM$MgCl_2$ for 20 min, followed by quenching in 50 mM NH_4Cl for 10 min and 3 washes with PBS. Cells were stained with DAPI and LD540 for 20 min at RT. Cells were kept in PBS and imaged within 24 h of fixation. Z-stacks spanning the whole cell (step size 0.3 µm) were acquired with Nikon Eclipse Ti-E microscope, 60X PlanApo VC oil objective NA 1.4 with 1.5x zoom. Image stacks were deconvolved using Huygens (Scientific Volume Imaging) batch processing application, and deconvolved image stacks were maximum intensity projected in MATLAB. Analysis of LD sizes/cell was performed as described in detail in (Salo et al., 2019), using CellProfiler and custom-made MATLAB scripts. For the data in Fig 6A, cells were immunostained with anti-Xpress (1:500) and Alexa-647 (1:400) antibodies as described (Salo et al. 2019), and fields of view with antibody staining positive cells were imaged.

DEV preparation

In vitro experiments were performed in the following HKM buffer: 50 mM Hepes, 120 mM Kacetate, and 1 mM MgCl2 (in Milli-Q water) at pH 7.4 and 275 ± 15 mOsm. All GUVs were composed of 99% DOPC (Avanti polar lipids, Inc), 0.5% (w/w) Rhodamine-DOPE, and 0.5% (w/w) biotinyl-DOPE. GUVs were prepared by electro-formation (Thiam et al. 2013). Phospholipids and mixtures thereof in chloroform at 0.5 µM were dried on an indium tin oxide (ITO) coated glass plate. The lipid film was desiccated for 1 h. The chamber was sealed with another ITO coated glass plate. The lipids were then rehydrated with a sucrose solution (275 ± 15 mOsm). Electro-formation is performed using 100 Hz AC voltage at 1.0 to 1.4 Vpp and maintained for at least 2 h. This low voltage was used to avoid hydrolysis of water and dissolution of the titanium ions on the glass plate. GUVs were directly collected with a Pasteur pipette.

To prepare the TG artificial LDs (aLDs), 5 µL of the oil was added to 45 µL of HKM buffer. TG aLDs were composed of 99,5% triolein and 0,5% (w/w) TG-NBD. TG-SE aLDs labeled with NBD fluorescent SE were composed of 70% triolein, 29,5% (w/w) cholesteryl oleate and 0,5% (w/w) SE-NBD. TG-SE aLDs labeled with NBD fluorescent TG were 70% triolein, 29,5% (w/w) cholesteryl oleate, and 0,5% TG-NBD (w/w).

In each of these case, the oil/HKM buffer mixture was sonicated for 30sec in a bath sonicator to generate aLDs. To make DEVs, GUVs were incubated with the aLDs for 5 min. The GUV-aLDs mixture was then placed on a glass coverslip pretreated with 10 % (w/w) BSA and washed three times with buffer. Where indicated, (Figures 5G, S5G-I, S4D-F), Bodipy 493/503 was added to the bulk solution to label NLs.

To prepare the model membranes incorporating TG and TG-NBD (Figures S3A), we took advantage of formation giant multilamellar vesicles (GMV) during the electroformation of DOPC GUV. During the formation of DEVs, the GMVs also incorporate aLDs made of TG containing TG-NBD, as above. The GMV-aLDs mixture was then placed on a glass coverslip pretreated with 10 % (w/w) BSA and washed three times with buffer. LipidTox Deep Red was then added to the buffer to analyze LipidTox fluorescence signal versus TG-NBD signal (Figure S3A).

Micromanipulation

Micro-pipettes were made from capillaries with a micropipette puller (Sutter instrument model P-2000). Micromanipulation was performed with a micromanipulator Eppendorf TransferMan®

4r. Micro-pipettes were used to manipulate DEVs. The pipettes were incubated in a 5% BSA for 1 h prior to conducting experiments to prevent droplet and membrane from adherence to the glass.

Nanotube formation and radius modulation by micro aspiration

For pulling nanotubes from a DEV (or a GUV), streptavidin coated microspheres were added to the bulk on the glass coverslip. Then, the DEV was gently captured by one of the two micro-pipettes to control surface tension of the DEV (see section below). One streptavidin coated microsphere was caught by the other micro-pipette and it was slowly moved toward the DEV. Upon contact, the biotinylated phospholipid of the DEV interacted strongly to the streptavidin coated microsphere surface. Finally, a nanotube was pulled by removing slowly the micro-pipette at the opposite direction to the DEV. The radius of the tube was modulated by altering the surface tension of the DEV.

$$R_t = \sqrt{\frac{\kappa}{2\gamma}}$$

Where κ is the bending rigidity of the DOPC membrane.

Nanotube radius measurements with fluorescence calibration

We vary the tube length at constant surface tension, which keeps the radius constant based on the previous equation. Therefore, for a given tension, we have many couples of tube length (L_t) and tongue length (L_p) in the micropipette (see Figure S4A). The conservation of surface yields

$$L_p = a.L_t + b$$

Thus, from this conservation, we can extract the slope (*a*) by measuring different couples of L_p and L_t.

On the other hand, conservation of the volume of the system links the radius of the tube to that of the of the GUV (R_g) and the pipette through the following equation (Hochmuth and Evans, 1982):

$$R_t = a.\left(1 - \frac{R_p}{R_g}\right).R_p$$

We measured different values of R_t, according to the above formula, and determined the associated Rh-DOPE intensity on the tube, normalized by the signal on the GUV. Thereupon,

we established a calibration curve enabling us to determine the tube radius by measuring the fluorescence intensity of Rh-DOPE.

Surface tension measurements

Surface tensions were also measured. Using Laplace's law, and the measurement of the pipette inner radius (R_p), DEV (or GUV) radius (R_g), and suction pressure, the surface tension of the interface was calculated:

$$\gamma = \frac{\Delta P_{suc}}{2\left(\frac{1}{R_p} - \frac{1}{R_g}\right)}$$

where ΔP_{suc} is the suction pressure. The suction was carried out using a level of water (precision 0.005 mm). The resulting pressure was measured with the water level variation between the zero (no aspiration and no ejection of buffer) and the aspiration of a DEV tongue in the micropipette. The nanotubes were pulled and modulates by changing surface tension between 5.10^{-1} mN/m and 10^{-3}mN/m.

Tube modulation and TG distribution experiments

The oil distribution measurements in membrane nanotubes (Figure 4), were done by changing very slowly the tube radius step by step, typically every 20 s. For nucleation experiments (Figures 5E-I, S5D-H), the nanotube diameter was decreased spontaneously from a value above 160 nm to values below 140 nm. For Figure 5H, the total number of nucleation events observed was counted and plotted as a function of the final nanotube radius. For Figure 5I, each time the nanotube radius was decreased drastically, it was considered as a trial, and if a nucleation event was observed, it was considered as a success event. The nucleation frequency corresponds to the number of success events divided by the number of trials.

FRAP experiments

FRAP experiments on ER-vesicles (Figure 3E) were performed on vesicles of around 10 µm in size and on their middle plane. FRAP experiments on nanotubes (Figures 5A-C) were performed by bleaching the signal on entire nanotubes (radii between 30 and 60 nm) to ensure unidirectional recovery of the fluorescence from molecules in the GUV. Planar membrane FRAP experiments on DEVs (Figures S5A-C) were performed by bleaching the apex of the DEV. Rh-DOPE and TG-NBD or SE-NBD signals were bleached simultaneously. The fluorescence signal recovery was monitored. GraphPad Prism was used to fit the FRAP recovery curves with a non-linear regression and the exponential « one-phase association model ».

Image analysis of swelling experiments and in vitro studies

Images were analyzed using image J software. For analysis of seipin enrichment in different sized ER-derived vesicles, (Figures 1J and S1H), fluorescence profiles were drawn perpendicular to ER-derived vesicles, averaged over 10 pixels for large objects and the full size of the objects was considered when they were small. The peaks of the profiles were measured. Peak values for both YFP-seipin and sec61ß-were recorded, seipin enrichment values indicate the seipin/sec61 fluorescence intensity ratio. The sizes of the analyzed vesicles were also measured and plotted. Vesicles which were below the resolution limit of the imaging setup were grouped at 0.2 µm in Figure 1J. Finally, the values were normalized so that 1 indicates the minimum seipin enrichment ratio.

For Figure 2F, LDs (stained by Bodipy-C_{12} or LipidTox deep red) in the entire cells were counted and we determined the fraction of LDs in contact with micrometric-sized vesicles (D > 1µm). We also determined the total signal of YFP-seipin and sec61ß-mCherry fluorescence on submicrometric and micrometric-sized vesicles. For both category of vesicles, the number of LDs were normalized to either sec61ß or seipin signal Figure 2G,I. In Figure 2H, YFP-seipin over sec61ß-mCherry signal ratio was represented for submicrometric to micrometric-sized membrane.

For Figure 3A-B, a fluorescence profile was drawn perpendicular to the micrometric-sized ER-vesicles and averaged over 10 pixels. The LipidTox fluorescence intensity of the peak was recorded on ER-vesicles before OA addition and t = 15 min after OA addition on the same ER-vesicles. The values in Figure 3B are normalized by the mean value of the LipidTox fluorescence of vesicles before OA addition.

For Figure 3C-D, a fluorescence profile was drawn perpendicular to the micrometric-sized ER-vesicles and averaged over 10 pixels. The Bpy-C_{12} fluorescence intensity of the peak was recorded on ER-vesicles at t = 20 min and t = 35 min on the same ER-vesicles. The values in Figure 3D are normalized by the mean value of the Bpy-C_{12} fluorescence intensity of the vesicles at t = 20 min. For figure S3E-F, a fluorescence profile was drawn perpendicular to the micrometric-sized ER-vesicles and the plasma membrane. It was averaged over 10 pixels. The Bpy-C_{12} and LipidTox fluorescence intensity of the peak was recorded after OA addition. The values in Figure S3F are normalized by the fluorescence intensity mean value of ER-vesicles for both LipidTox and Bpy-C_{12} signals.

For figure S3G-H, a fluorescence profile was drawn perpendicular to the micrometric-sized ER-vesicles and the newly formed LDs. It was averaged over 10 pixels for the ER vesicles and 5 pixels for the LDs. The Bpy-C_{12} and LipidTox fluorescence intensity of the peak was recorded after OA addition. The values in Figure S3G are normalized by the mean value of the fluorescence intensity of ER-vesicles for both LipidTox and Bpy-C_{12} signals.
For TGs concentration analysis in ER-vesicles (Figure 3F), a fluorescence profile was drawn perpendicular to each vesicle. The maximum was taken for both Bpy-C_{12} and sec61ß-mcherry. TG concentrations in the ER membrane was considered as the fluorescence ratio between Bpy-C_{12} and sec61ß-mcherry. The TG concentrations in submicrometric and micrometric-sized membranes were plotted in Figure 3G and all values are normalized by the mean TG concentration in the micrometric-sized membranes. Figure 3I follows the same quantification protocol as Figure 2F,G.

For oil distribution measurements (Figure 4) between planar and curved membranes, a fluorescence profile was drawn perpendicular to the nanotube and averaged over several microns, the maximum of this profile which corresponds to the fluorescence of the tube was taken (for both NBD and Rhodamine) (Figure 4C). These two values are normalized by the mean fluorescence of the GUV. The oil enrichment values (Figures 4D-E and G-H) corresponds to the ratio of NBD over Rhodamine fluorescence signals and are normalized by the concentration of oil in the planar membrane.

For Figure 5, the fluorescence intensity of the nanotubes and artificial nucleated droplets were recorded with a profile averaged over the size of the nucleated droplet, and normalized by the fluorescence in the DEV, for both NBD (or Bodipy) and Rhodamine signals.

Statistics

Statistical comparisons where made using a non-parametric t-test (GraphPad Prism; *** indicates $p < 0.0001$ ** indicates $p < 0,001$ * indicates $p < 0.01$). Unless mentioned, all values shown in the text and Figures are mean ± S.D.